Dynamic shear rupture interactions with fault bends and off-axis secondary faulting

Alexei N. B. Poliakov

Laboratoire de Geophysique et Tectonique, CNRS, Université Montpellier II, Montpellier, France

Renata Dmowska and James R. Rice

Department of Earth and Planetary Sciences and Division of Engineering and Applied Sciences, Harvard University, Cambridge, Massachusetts, USA

Received 19 April 2001; revised 25 January 2002; accepted 30 January 2002; published 15 November 2002.

[1] On the basis of elastodynamic stress fields for singular crack and nonsingular slip-weakening models of propagating rupture, we develop preliminary answers to such questions as follows: If a rupturing fault is intersected by another, providing a possible bend in the failure path, when will stressing be consistent with rupture along the bend? What secondary fault locations and orientations, in a damaged region bordering a major fault, will be stressed to failure by the main rupture? Stresses that could initiate rupture on a bend are shown to increase dramatically with crack speed, especially near the limiting speed (Rayleigh for mode II, shear for mode III). Whether a bend path, once begun, can be continued to larger scales depends on principal stress directions and ratios in the prestress field. Conditions should often be met in mode II for which bend paths encouraged by stressing very near the rupture tip are discouraged by the larger-scale stressing, a basis for intermittent rupture propagation and spontaneous arrest. Secondary failure in the damage zone likewise increases markedly as the limiting speed is approached. Such may make the fracture energy much greater than for slip on a single surface. The extent of secondary faulting is strongly affected by prestress directions and the ratio of residual to peak strength. For mode II, prestress controls whether activation occurs primarily on the extensional side, which we show to be the typical case, or on the compressional side too. Natural examples are consistent with the concepts developed. *INDEX TERMS:* 7209 Seismology: Earthquake dynamics and mechanics; 7260 Seismology: Theory and modeling; 8020 Structural Geology: Mechanics; 8168 Tectonophysics: Evolution of the Earth: Stresses—general; 7230 Seismology: Seismicity and seismotectonics; *KEYWORDS:* fault mechanics, fault branching, rupture dynamics, earthquakes

Citation: Poliakov, A. N. B., R. Dmowska, and J. R. Rice, Dynamic shear rupture interactions with fault bends and off-axis secondary faulting, *J. Geophys. Res.*, *107*(B11), 2295, doi:10.1029/2001JB000572, 2002.

1. Introduction

1.1. Observations

[2] Earthquakes seldom rupture along single planar faults. Instead, there exist geometric complexities, including fault bends, branches and step overs, which affect the rupture process, including nucleation and arrest. Starting in the 1970s and 1980s systematic field observations have shown the importance of such complexities for determining the size of an earthquake and strong motion generation. The role of fault bends in the initiation and termination of rupture was noted, with many examples, by *King and Nabelek* [1985], who proposed that rupture in individual earthquakes is often limited to regions between bends in faults. The epicenter of the M_s 6.5 1966 Parkfield earthquake was close to a 5° bend, and rupture stopped after propagation past a bend and offset. The M_s 7.5 1973 earthquake in Luhuo, China, had an epicenter near a bend. The M_s 6.7 1975 Lice, Turkey, earthquake started near a bend in the fault and terminated near another one. The bilateral M_s 7.8 1976 Tangshan, China, earthquake had an epicenter located at a bend in the aftershock distribution and terminated at the southern end by thrust faulting. The M_s 7.4 Caldiran, Turkey, earthquake started at a pronounced 40° bend. The M_s 5.7 1979 Coyote Lake, California, earthquake had an epicenter near a bend in Calaveras fault; the rupture terminated adjacent to a dilational jog.

[3] More field observations of rupture interaction with fault bends and jogs were discussed by *King* [1986] and *Sibson* [1985, 1986]. These include the 1979 Imperial Valley and 1992 Landers, California, earthquakes discussed in the closing section of the paper, and the 1968 M_s 7.2 Dasht-e-Bayaz earthquake in NE Iran, where the rupture continued through two 1-km-broad dilational jogs in a highly irregular manner, decelerating and pausing at the jogs, so the overall average rupture velocity was only 0.5 km/s [*Niazi*, 1969].

0148-0227/02/2001JB000572$09.00

[4] Broad observations of strike-slip fault complexities in the fault systems of Turkey have been collected by *Barka and Kadinsky-Cade* [1988] and worldwide by *Knuepfer* [1989] and *Aydin and Schultz* [1990]. Dynamic finite difference modeling of vertical strike-slip ruptures jumping an offset was introduced, just in time for the 1992 Landers event, by *Harris et al.* [1991] and *Harris and Day* [1993]. That has recently been extended to a dynamic model of the rupture of the complex M_w 7.4 1999 Izmit, Turkey, earthquake [*Harris et al.*, 2002]. The models confirmed the highly irregular rupture velocity and slip in the progression of strike-slip failure through fault offsets, as well as the importance of fault steps in rupture arrest. The modeling also recognized the importance of past earthquake history, which contributes to the prestress and can be decisive for determining if a given offset is breached [*Harris and Day*, 1999].

[5] In dip-slip regimes, less information is usually available on geometrical complexities. However, the rupture processes of some modern continental thrust earthquakes are inferred from mapped surface ruptures complemented by seismological observations. The *M* 7.6 1952 Kern County earthquake exhibited a 1-km strike-slip offset between two thrust segments [*Buwalda and St. Amand*, 1955]. The *M* 6.8 1968 Meckering, Australia, earthquake jumped a 3-km right step via a strike-slip fault that displayed surface rupture [*Gordon and Lewis*, 1980]. Surface rupture of the *M* 6.4 1971 San Fernando earthquake showed a 1.5-km offset between thrust segments [*Tsutsumi and Yeats*, 1999]. The *M* 7.3 1980 El Asnam, Algeria, earthquake jumped a 2-km tear fault offset defined by surface rupture and aftershock focal mechanisms [*King and Yielding*, 1984]. The *M* 5.5 1982 New Idria, *M* 6.5 1983 Coalinga, and *M* 6.1 1985 Kettleman Hills thrust earthquakes were single segment events on a blind thrust fault [*Ekstrom et al.*, 1992]; see closing section. Folds above the thrust are offset by 2 and 4 km, suggesting similar offsets in the thrust faults; aftershock focal mechanisms suggest that a lateral ramp occupies the 4-km-wide offset [*Eaton*, 1990]. The *M* 5.9 1987 Whittier Narrows earthquake was a single segment blind thrust main shock with aftershocks illuminating a strike-slip fault along the edge of the main shock rupture zone. The strike-slip fault apparently confined the main shock rupture. The *M* 6.7 1994 Northridge earthquake may have been confined in the 7- to 15-km depth range by two lateral ramps that offset the Santa Susanna fault zone by 2- and 5-km at the surface [*Yeats et al.*, 1994; *Hauksson et al.*, 1995].

[6] *Magistrale and Day* [1999] performed three-dimensional (3-D) finite difference simulations of earthquake rupture to evaluate the effectiveness of lateral ramps or tear faults joining the thrust segments in retarding rupture. They concluded that with a tear fault or lateral ramp present, and necessarily being modeled as being orthogonal to the main fault due to constraints in their finite difference procedure, offsets up to 2 km wide usually present little impediment to rupture, and offsets 2 to 5 km are more significant barriers that may or may not rupture. Absent a tear fault, the maximum offset that can be breached is an order of magnitude smaller. More simulations of this kind are presented by *Magistrale* [2000], investigating the influence of fault strength, stress drop, hypocenter location, stress heterogeneity, etc., on the rupture of two thrust segments connected by an orthogonal tear fault. There is also evidence for the branching of rupture path in crustal thrust events as a deeply nucleated event propagates up dip, e.g., in the 1971 San Fernando earthquake as suggested by *Heaton and Helmberger* [1979]; see closing section.

1.2. Stress Near a Fast Propagating Fracture

[7] Dynamic effects strongly distort elastically predicted stress fields near rapidly propagating crack tips. The generic effect is that of the maximum off-fault shear stress increases, relative to that on the main fault plane, with the velocity v_r of rupture propagation. This increase becomes strikingly large at high speeds, i.e., when *vr* approaches the "limiting speed" $c_{\lim}$, which is the shear speed c_s for mode III and the Rayleigh speed c_R ($\sim$0.92 c_s) for mode II. It has long been suggested [e.g., *Andrews*, 1976a; *Rice*, 1980] (also B. V. Kostrov, orally reported results, Bad Honnef, Germany, 1978, as cited by *Rice* [1980]) that these high off-fault stresses could play a central role in the dynamics of the rupture process. They should contribute to secondary faulting within the damaged border zones which are known to occur along major faults [*Wallace and Morris*, 1986; *Power et al.*, 1988], like along the exhumed San Gabriel [*Chester et al.*, 1993] and Punchbowl [*Chester and Chester*, 1998] faults. They may also contribute to bifurcation of the fracture along a kinked path or, at least, generation of a highly intermittent rupture propagation. The expected scenario is for the rupture to speed up toward $c_{\lim}$, which is the basic fate of a rupture confined to a plane [e.g., *Freund*, 1990], but in so doing to generate the high off-fault stress which make the rupture tip susceptible to bending or forking. That bifurcation can either stop the rupture completely, or can lead to a temporary slowdown until something more resembling the static stress distribution gets established again, and re-nucleates continuing rupture on the main fault plane. That provides new ways of thinking about the origin of small earthquakes and the frequency-magnitude relation because it provides a way to stop ruptures without recourse to assuming strong heterogeneity along the main fault zone itself and provides a route to understanding the enriched high frequency content of strong ground motion. Also, dissipation in secondary faulting provides a way of understanding why the inferred fracture energy of large earthquakes is orders of magnitude larger than what is inferred from laboratory shear failure even of initially intact rock [*Rice*, 1980; *Wong*, 1982], and indeed why earthquake fracture energies are so large that we cannot easily explain from them how small earthquakes could even nucleate.

1.3. Numerical Modeling of Dynamic Rupture

[8] The effect of those high off-fault stresses is well illustrated in simulation by boundary integral methodology of the spontaneous growth of a dynamic shear crack without constraints on the crack tip path, as performed by *Kame and Yamashita* [1999a, 1999b]. The methodology enables them to handle complicated fault geometries such as bends and branches. Kame and Yamashita base the choice of the orientation of each new increment of crack path on the maximum shear stress along radial directions very near the crack tip, explicitly including the high-speed distortion of the stress field. It remains an open issue of how to properly include effects of normal stress in that description. Nevertheless, the results based on the near-tip shear stress

show that when high speed is attained, the crack tip forks and each fork bends, so much so that the rupture ultimately arrests. The nature of their crack-tip-focused procedure does not allow for the possibility of renucleation of rupture on the main fault plane, which we think is a critical feature for the overall rupture dynamics. That, the inclusion of normal stress effects in the failure criterion, and the channeling of allowable paths along preexisting planes of a fault network are important additional issues to address.

[9] Previous 2-D works that simulated spontaneous dynamic rupture propagation on preexisting nonplanar faults, with different boundary integral equation formulations, were done by *Koller et al.* [1992], *Tada and Yamashita* [1996, 1997], *Kame and Yamashita* [1997], and *Bouchon and Streiff* [1997]. *Seelig and Gross* [1999] did analogous studies of branching tensile cracks. *Tada et al.* [2000] have formulated boundary integral equations for arbitrary 3-D nonplanar faults removing any singularities in the time domain, and *Aochi et al.* [2000a, 2000b] simulated spontaneous rupture process on a complex branching fault. *Aochi and Fukuyama* [2002] applied such an approach to understanding the 1992 Landers earthquake. That work also based the failure criterion on only the shear stress at the rupture tip, although very recently, *Aochi et al.* [2002] have extended this approach to include the effects of normal stresses as well.

[10] Finite element procedures have also been developed for predominantly tensile failures with dynamically self-chosen rupture paths, allowing the possibility of multiple paths and path competition. These include models in which elements lose stiffness with deformation [*Johnson*, 1992] and those in which all or some subset of element boundaries are potential failure surfaces on which coupled tensile decohesion and slip weakening can take place [*Xu and Needleman*, 1994; *Camacho and Ortiz*, 1996; *Falk et al.*, 2001]. Such models have not yet been extended to dynamic fault ruptures.

1.4. Objectives of the Present Work

[11] The preceding discussion points to the major problem in rupture dynamics of understanding propagation through geometrically complex fault systems containing bends, branches, step overs and, in the case of major faults, an array of smaller faults or fractures in damaged border regions. Our aim here is to study the stress field near a dynamically propagating rupture, as described by both singular elastic crack models and by a version of slip-weakening rupture models (analyzed in a preliminary way by *Rubin and Parker* [1994]). We use those results to suggest what may control whether a rupture will branch along a kinked path and to identify the nature and extent of secondary faulting expected in damaged border zones. We find that important parameters are the rupture speed as well as the principal directions and ratios of components in the prestress field through which the rupture propagates.

2. Elastodynamic Singular Crack Solutions and Application to Fault Bends

[12] We consider the special, but reasonably general, situation in which the state of tectonic prestress σ^o_{ij} is such that the fault plane ($y = 0$) is parallel to the intermediate principal stress direction. Further, we assume that the direction of slip aligns with the shear traction direction on that plane, hence is perpendicular to the intermediate direction. The direction of rupture propagation may take any orientation relative to the slip direction. We label that propagation direction as the x direction and make two simple choices for it: (1) A mode II configuration (Figure 1a) in which the rupture direction and slip direction coincide, both in the x direction, so that the prestress has the form

$$\sigma^o_{ij} = \begin{bmatrix} \sigma^o_{xx} & \sigma^o_{yx} & 0 \\ \sigma^o_{yx} & \sigma^o_{yy} & 0 \\ 0 & 0 & \sigma^o_{zz} \end{bmatrix},$$

where the z direction is the intermediate direction; and (2) a mode III configuration in which the rupture direction (x) and slip direction (z) are perpendicular, so that the prestress is

$$\sigma^o_{ij} = \begin{bmatrix} \sigma^o_{xx} & 0 & 0 \\ 0 & \sigma^o_{yy} & \sigma^o_{yz} \\ 0 & \sigma^o_{yz} & \sigma^o_{zz} \end{bmatrix},$$

and now the x direction is the intermediate principal stress direction.

[13] For simplicity, we start from the study of elastic singular solutions around a shear crack tip propagating with velocity v_r (Figure 1a for mode II) and sustaining a uniform residual stress shear stress τ_r along the slipping rupture surface.

2.1. Mode II

[14] Mode II rupture occurs at the extremities of the slipping zone along strike for strike-slip faulting, and along dip for dip-slip faulting. The initial stress state σ^o_{ij} is depicted on the right in Figure 1a. The stress change due to presence of the crack is

$$\Delta\sigma_{ij} = \frac{K_{\mathrm{II}}}{\sqrt{2\pi r}} F^{\mathrm{II}}_{ij}(\theta, v_r) + \begin{bmatrix} 0 & -\Delta\tau \\ -\Delta\tau & 0 \end{bmatrix} + O(\sqrt{r}),$$

where the reduced matrix represents just the xx, yy, and xy components, $\Delta\tau = \sigma^o_{yx} - \tau_r$ is the stress drop, $K_{\mathrm{II}} \propto \Delta\tau\sqrt{L}$ is the stress intensity factor, L is the length of the slipping region, and r, θ are polar coordinates with origin at the crack tip (Figure 1b). The form of the $F^{\mathrm{II}}_{ij}(\theta, v_r)$ are given in Appendix A, equations (A5), and by *Freund* [1990]. The symbol $O(\sqrt{r})$ represents additional terms, which are part of the full solution but which vanish at least as fast as $\sqrt{r}$ at the crack tip.

[15] The final stress σ_{ij} is the sum of the initial σ^o_{ij} and stress change $\Delta\sigma_{ij}$:

$$\sigma_{ij} = \sigma^o_{ij} + \Delta\sigma_{ij} = \frac{K_{\mathrm{II}}}{\sqrt{2\pi r}} F^{\mathrm{II}}_{ij}(\theta, v_r) + \begin{bmatrix} \sigma^o_{xx} & \tau_r \\ \tau_r & \sigma^o_{yy} \end{bmatrix} + O(\sqrt{r}).$$

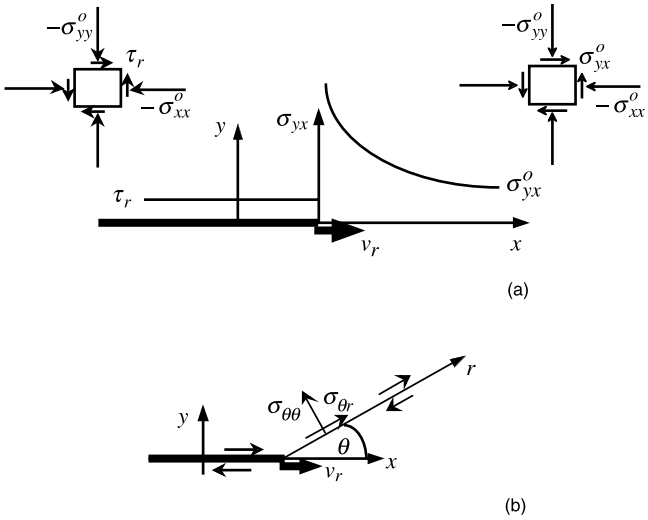

Figure 1. (a) Singular elastic crack model of a mode II shear rupture propagating with velocity v_r. Stress state shown (left) far behind the tip and (right) far ahead. (b) Stresses ($\sigma_{\theta\theta}, \sigma_{\theta r}$) on a branched fault plane originating at the rupture tip at angle θ.

With inclusion of the $O(\sqrt{r})$ terms, this would of course agree with σ^o_{ij} far from the crack. We shall later use the notation σ^1_{ij} to denote the finite stress state, like in the middle term above, which provides the first correction near the rupture tip to the $1/\sqrt{r}$ singular term. In order to discuss potential bending or forking of the crack, it is relevant to consider the normal and tangential stresses ($\sigma_{\theta\theta}, \sigma_{\theta r}$) on a potential plane originated at the crack tip at angle θ (Figure 1b). To find how much shear stress $\sigma_{\theta r}$ is different from the critical stress needed to overcome shear resistance $-f\sigma_{\theta\theta}$ (f is the friction coefficient) on the crack, we also plot the Coulomb stress, equal to $\sigma^{\text{Coul}}_{\theta r} = \sigma_{\theta r} + f\sigma_{\theta\theta}$, where a positive value of $\sigma^{\text{Coul}}_{\theta r}$ means that slip is encouraged.

2.1.1. Influence of the Rupture Velocity on the Near-Tip Stress

[16] The initiation of a bifurcation of the rupture path onto a bend direction will presumably be controlled by stresses very near the rupture tip, and hence by characteristics of the $1/\sqrt{r}$ singular field, in such crack models. Features of the stress field at larger scales will, however, determine whether the rupture, once nucleated on a bend path, can continue long distances along it. Because the singular part of the stress depends only on θ for fixed r, all stresses are normalized by $K_{\text{III}}/\sqrt{2\pi r}$. The singular term is strongly influenced by rupture velocity. Figure 2 shows the dependence of normalized $\sigma_{\theta\theta}$, $\sigma_{\theta r}$, and $\sigma^{\text{Coul}}_{\theta r}$, including the singular $1/\sqrt{r}$ terms only, on the angle θ for different velocities of crack propagation, measured as fractions of the shear (c_s) or Rayleigh (c_R) velocities. The main feature of dynamic crack propagation is that the stresses off the main fault plane grow relative to those on it as the crack velocity increases. The normal stress $\sigma_{\theta\theta}$ does not qualitatively change very much with the increase of v_r (it is asymmetric; more extensional for negative θ and more compressive for positive θ). At the same time, the shear stress $\sigma_{\theta r}$ evolves from having one maximum at $\theta = 0°$ for $v_r = 0^+$ to having two maxima at $\theta \approx \pm 70°$ for higher velocities ($v_r > 0.85c_R$), as shown already by *Kame and Yamashita* [1999a, 1999b]. These maxima grow strongly with increase of v_r. As a result the Coulomb stress $\sigma^{\text{Coul}}_{\theta r}$ also has a one maximum for $v_r < 0.9 - 0.95c_R$ (Figure 3a) suggesting that the propagating fault will bend at this regime at angles $-10° < \theta < -70°$ depending on the velocity of propagation. The higher the velocity is, the higher the most favored bending angle is. While $\sigma^{\text{Coul}}_{\theta r}$ is highest on the extensional side of the rupture (negative θ), it is also elevated on the compressional side. If $v_r > 0.95c_R$, there will be two strong maxima at $\theta \approx \pm 70°$, suggesting that there could be a fracture bifurcation or forking.

[17] The discussions of this paper neglect pore fluid presence, which will tend to buffer the effect of changes in normal stress on the Coulomb stress. Correspondingly, we have used a value of f chosen toward the lower end of the range suggested by laboratory and borehole observations ($f = 0.60$ in Figures 2 and 3a, $f = \tan 30° \approx 0.58$ in the subsequent slip-weakening analysis). However, fuller inclusion of pore fluid effects does not seem to qualitatively change our conclusions. *Cocco and Rice* [2002] showed that when stress changes from a nearby earthquake are suddenly imposed on a thin neighboring fault, which fault does not significantly perturb those stress changes outside its core, then the undrained pore pressure change Δp in the core, when it has isotropic poroelastic properties, is a Skempton coefficient B [*Rice and Cleary*, 1976] times a linear combination of the changes in normal stress and mean stress (i.e., first stress invariant) of that imposed field. In the limit for which the shear rigidity of the fault core is much less than outside it (and also in the limit of a highly anisotropic damage distribution as discussed by *Cocco and Rice* [2002]), this reduces for a branch fault orientation like in Figure 1b to $\Delta p = -B\Delta\sigma_{\theta\theta}$. In the opposite limit, for which the fault core properties are identical to those outside it, the relation is $\Delta p = -B(\Delta\sigma_{rr} + \Delta\sigma_{\theta\theta} + \Delta\sigma_{zz})/3$. Taking representative values $f = 0.75$ and $B = 0.50$ [*Cocco and Rice*, 2002], it is clear that in the first limit the results for Coulomb stress will be of the form $\sigma_{\theta r} + f'\sigma_{\theta\theta}$ with $f' = f(1 - B) \approx 0.38$ and hence will be qualitatively similar to what is shown in Figures 2 and 3a. The results for the second limit are shown in Figure 3b, and it is clear that qualitatively, the conclusions remain the same; branches to both sides are favored at high speeds, but there is a preference for branching to the extensional side. We have also checked intermediate cases in which both normal stress and mean stress changes affect p and reach the same conclusion.

2.1.2. Influence of the Stress Field at Larger Scales

[18] This can be crucial for the continuation of rupture, once begun, along a kinked path. Consider a volume of rock under maximum and minimum compressive principal stresses, $S_{\max}$ and $S_{\min}$, like in Figure 4. The ratio of $S_{\min}$ to $S_{\max}$ defines an angle ϕ (not to be confused with a critical Mohr-Coulomb failure angle, with which it would coincide only if the rock was noncohesive and was stressed to failure). Relative to the principal directions, there are two quadrants of fault orientations for which right-lateral slip is encouraged by the shear stress, as marked in Figure 4. Also, the orientation sustaining the maximum ratio of right-lateral shear stress, τ, to compressive normal stress, $-\sigma$, makes an

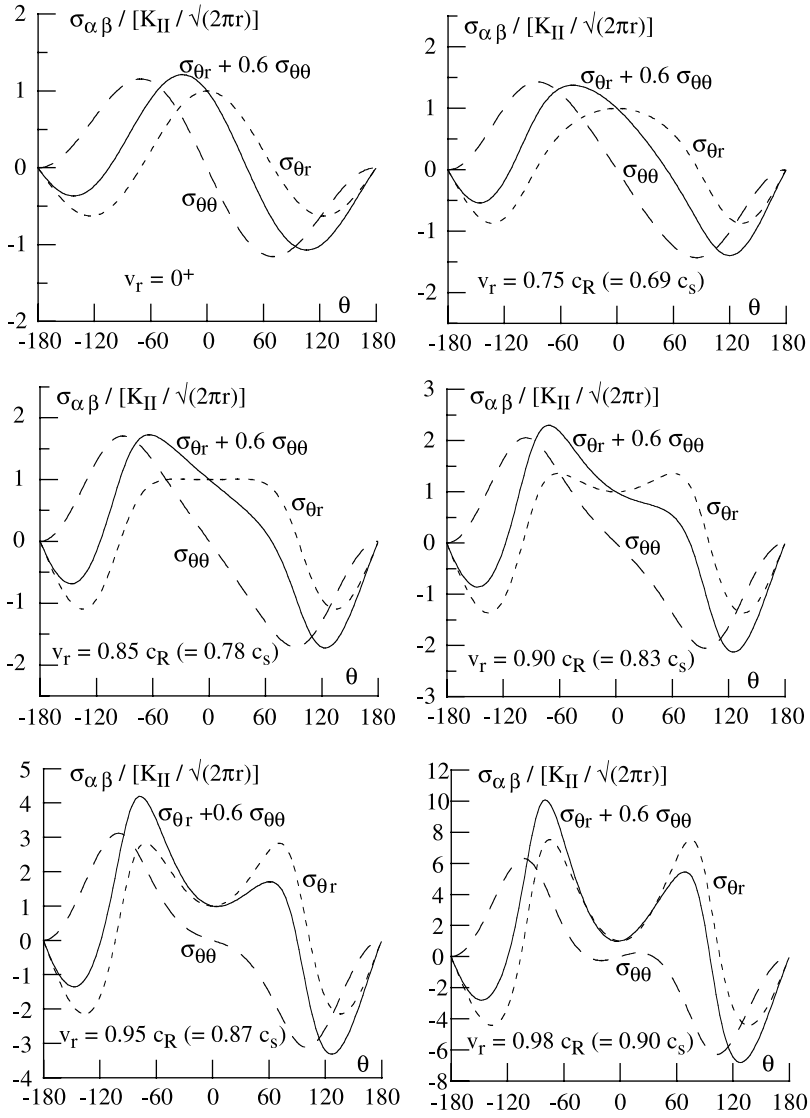

Figure 2. Dynamic crack tip singular fields for right-lateral mode II rupture at different rupture speeds v_r.

angle of $(\pi/4) - (\phi/2)$ with the direction of maximum compression.

[19] Now let us apply that concept to stressing along a bend path. We observe that the first correction to the $1/\sqrt{r}$ singular term involves the uniform stress field

$$\sigma_{ij}^{1} = \begin{bmatrix} \sigma_{xx}^{o} & \tau_r \\ \tau_r & \sigma_{yy}^{o} \end{bmatrix},$$

and so we could identify $S_{\min}$ and $S_{\max}$ as the principal stresses of that field, to understand how that correction σ_{ij}^{1} influences the stresses that drive faulting. At larger distances from the crack tip the stress field approaches the prestress σ_{ij}^{o}, so at such distances we would wish to identify $S_{\min}$ and $S_{\max}$ with principal values of σ_{ij}^{o}.

[20] With either interpretation there are two distinct limiting regimes, depending on the ratio of the fault parallel precompression, $-\sigma_{xx}^{o}$, to the fault-normal precompression, $-\sigma_{yy}^{o}$. The fault-parallel compression is greater in Figure 5a, and the fault-normal in Figure 5b. To see what divides these cases, first consider the situation $\sigma_{xx}^{o} = \sigma_{yy}^{o}$. Then both the $S_{\max}$ for the prestress σ_{ij}^{o}, and the $S_{\max}$ for the first-correction stress σ_{ij}^{1}, make an angle $\psi = 45°$ with the fault plane. However, when $(-\sigma_{yy}^{o}) < (-\sigma_{xx}^{o})$, like in Figure 5a, the $S_{\max}$ based on σ_{ij}^{o} makes an angle ψ smaller than 45° with the fault plane, and the $S_{\max}$ based on σ_{ij}^{1} makes a yet smaller angle ψ (since $\tau_r < \sigma_{yx}^{o}$). If the residual stress τ_r during earthquake slip approaches zero (complete stress drop), then ψ based on σ_{ij}^{1} approaches zero. In comparison, when the fault-normal precompression is dominant, so that $(-\sigma_{yy}^{o}) > (-\sigma_{xx}^{o})$ like in Figure 5b, then the $S_{\max}$ based on σ_{ij}^{o} makes an angle ψ greater than 45° with the fault, and the ψ based on σ_{ij}^{1} makes a yet steeper angle. That latter ψ; approaches 90° in the limit of complete stress drop. Those differences mean that different angular zones experience right-lateral shear stress, depending on whether the fault-normal precompression is smaller or larger than the fault-parallel component. The differences are most striking when we consider the first-correction stress state σ_{ij}^{1} for which the angle change, in the limit of complete stress drop, approaches 90°.

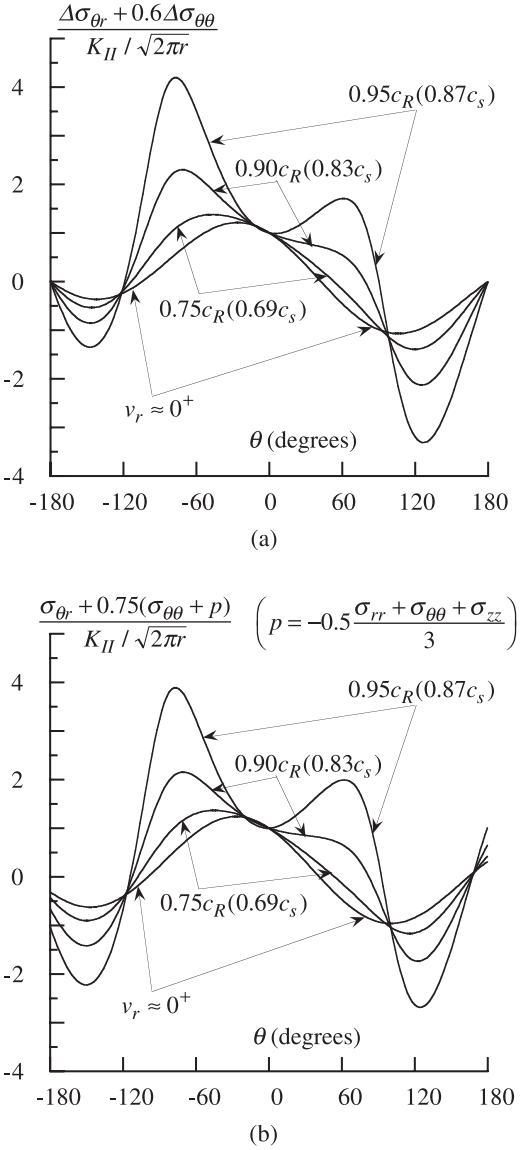

Figure 3. Coulomb stress $\sigma_{\theta r}^{\mathrm{Coul}} = \sigma_{\theta r} + f(\sigma_{\theta\theta} + p)$ of dynamic crack tip singular fields, for right-lateral mode II rupture at different rupture speeds v_r. (a) Pore pressure p neglected, like in Figure 2. (b) Case of identical poroelastic properties within the branch fault core as outside it.

[21] We expect that the stresses σ_{ij}^{1} determine, or at least strongly affect, whether the rupture along the bend path can be continued beyond the immediate vicinity of the rupture tip, where it nucleated under stresses like those plotted Figures 2 and 3. Similarly, the stresses σ_{ij}^{o} should control whether propagation can be continued far from the tip. Figure 5 thus predicts that when the fault-parallel precompression is large compared to the fault-normal precompression (Figure 5a), the stress state could allow rupture to continue along bend paths primarily to the compressional side (even though the compressional side is less favored for nucleation along a bend path), but would inhibit continuation on the extensional side. When the fault-normal precompression is instead the larger (Figure 5b), the stress state could encourage ruptures to continue

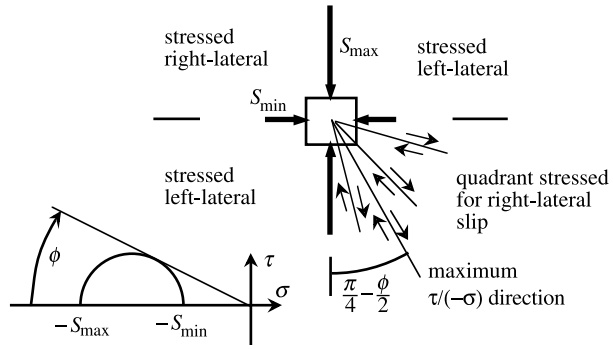

Figure 4. General stress state under maximum and minimum compressive principal stresses, $S_{\max}$ and $S_{\min}$. The ratio of $S_{\min}$ to $S_{\max}$ defines an angle ϕ, not to be confused with the critical Mohr-Coulomb angle.

on bend paths to the extensional side and inhibit the compressional.

[22] Because the dictates of the strongly velocity-dependent stress very near the rupture tip (Figures 2 and 3) will often be inconsistent with what the stress at larger scales (Figure 5) can sustain as a rupture, it is plausible to expect

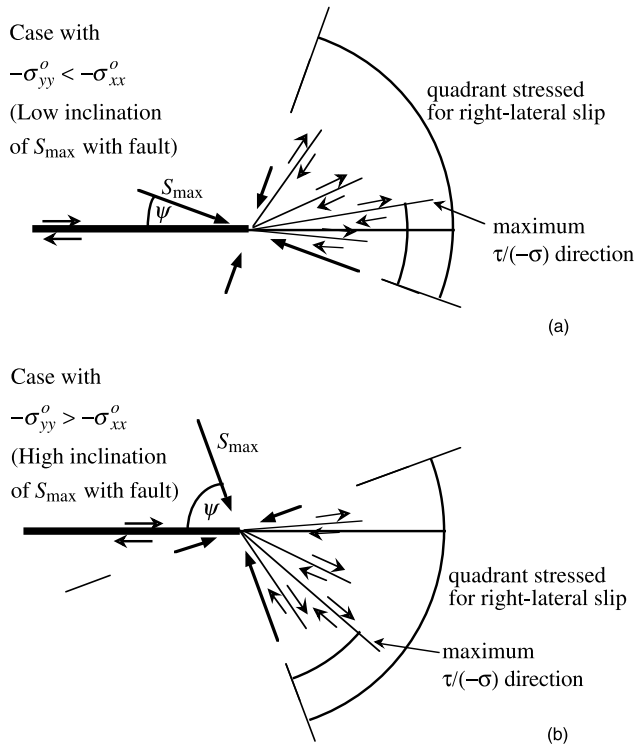

Figure 5. Qualitative prediction of the directions over which the larger-scale stress states (σ_{ij}^{1} or σ_{ij}^{o}) favor right-lateral shear along bend paths. (a) Fault-parallel precompression is dominant, $(-\sigma_{yy}^{o}) < (-\sigma_{xx}^{o})$: $S_{\max}$ makes an angle ψ smaller than 45° with the fault plane, allowing rupture to continue along bend paths primarily to the compressional side. (b) Fault-normal precompression is dominant, $(-\sigma_{yy}^{o}) > (-\sigma_{xx}^{o})$: ψ is greater than 45°, allowing rupture to continue on bend paths primarily to the extensional side.

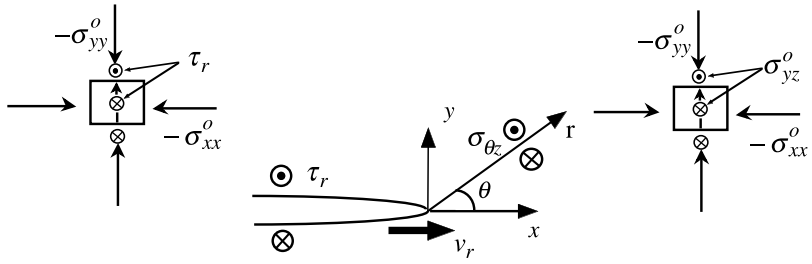

Figure 6. Singular elastic crack model of a mode III rupture propagating with velocity v_r.

that there will be many failed attempts to follow bend faults where they are available. Hence rupture propagation may be intermittent and subject to spontaneous self-arrest, e.g., in a manner analogous to that shown by *Kame and Yamashita* [1999a, 1999b]. The above discussion focused on the signs of the shear components of σ^1_{ij} and σ^o_{ij}. However, the magnitudes are also important; the driving shear stress must be greater than τ_r along the branch path.

[23] Because our considerations here have not explicitly modeled the alterations of the stress field due to actual rupture growth along a bend path, our conclusions are speculative. Nevertheless, they provide predictions, which could be tested by field observations (see the natural examples in the closing section here) and by detailed numerical simulation methods like those mentioned in the Introduction, of how rupture velocity and the nature of the prestress may control the propensity of rupture to follow a bend path. Some such relevant numerical simulations have been reported recently: N. Kame et al. (Effects of prestress state and rupture velocity on dynamic fault branching, submitted to *Journal of Geophysical Research*, 2002) used the boundary integral equation formulation of *Kame and Yamashita* [1999a, 1999b], applying it to a straight fault with a branch at 15° to one side or the other. They varied the incoming v_r and the prestress angle ψ (Figure 5) of $S_{\max}$ in the prestress field and verified that the size of that angle did indeed control whether branch paths to the extensional or compressional side would be followed. Also, *Aochi et al.* [2002] report simulations which show that the direction of branching is favored to the compressional side when faults are loaded close to the Coulomb frictionally optimal principal stressing directions relative to the main fault. In that case the $S_{\max}$ direction for σ^o_{ij} makes a shallow angle of $(\pi/4) - \arctan(f)/2$ with the fault, so that their simulation corresponds to the case shown in Figure 5a and the branching they found is consistent with the predictions made.

2.2. Mode III

[24] Mode III rupture (Figure 6) occurs at the extremities of the slipping zone along strike for dip-slip faulting, and along depth for vertical dip-slip faulting. The initial stress state, given earlier, is depicted on the right in the figure. The stress change associated with the crack is

$$\Delta\sigma_{ij} = \frac{K_{\mathrm{III}}}{\sqrt{2\pi r}} F^{\mathrm{III}}_{ij}(\theta, v_r) + \begin{bmatrix} 0 & 0 & 0 \\ 0 & 0 & -\Delta\tau \\ 0 & -\Delta\tau & 0 \end{bmatrix} + O(\sqrt{r})$$

with stress drop $\Delta\tau = \sigma^o_{yz} - \tau_r$ and $K_{\mathrm{III}} \propto \Delta\tau\sqrt{L}$. The form of the $F^{\mathrm{III}}_{ij}(\theta, v_r)$ is given by equations (A8) and by *Erdogan* [1968] and *Freund* [1990]. The final stress σ_{ij} is thus

$$\sigma_{ij} = \sigma^o_{ij} + \Delta\sigma_{ij} = \frac{K_{\mathrm{III}}}{\sqrt{2\pi r}} F^{\mathrm{III}}_{ij}(\theta, v_r) + \begin{bmatrix} \sigma^o_{xx} & 0 & 0 \\ 0 & \sigma^o_{yy} & \tau_r \\ 0 & \tau_r & \sigma^o_{zz} \end{bmatrix} + O(\sqrt{r}),$$

where now the middle term provides the first correction σ^1_{ij} to the $1/\sqrt{r}$ singular terms.

[25] To explore the possibility of crack forking or branching, we calculate the antiplane Coulomb stress $\sigma^{\mathrm{Coul}}_{\theta z}$ on a potential bend plane originating at the crack tip at an angle θ: $\sigma^{\mathrm{Coul}}_{\theta z} = \sigma_{\theta z} + f\sigma_{\theta\theta}$. The term proportional to $1/\sqrt{r}$ contains no diagonal elements and as a result, the $\sigma_{\theta\theta}$ stress does not contribute, so that $\sigma^{\mathrm{Coul}}_{\theta z} = \sigma_{\theta z}$ for that term. We normalize the singular term by $K_{\mathrm{III}}/\sqrt{2\pi r}$ and show it for different v_r/c_s values in Figure 7a. Similarly to mode II, $\sigma_{\theta z}$ has one maximum for lower velocities (approximately for $v_r/c_s < 0.7$) , while at higher velocities ($v_r/c_s > 0.7$) it has two maxima at $\theta \approx \pm 90°$. Because, these maxima are symmetric, the propagating fracture may fork rather than bend (in contrast to mode II fracture where the maximum shear stress on the extensional side is always higher than on the compressional). These features may be a source of intermittency in propagation and spontaneous arrest, like discussed for mode II.

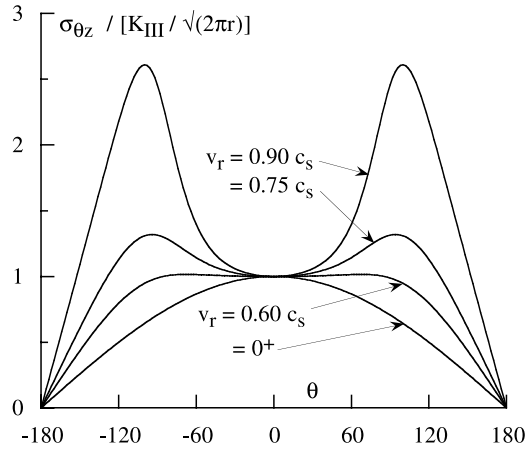

Figure 7. Dynamic singular fields for mode III at different v_r.

3. Slip-Weakening Dynamic Model

[26] An underlying assumption of singular crack models is that inelastic breakdown processes are confined to the immediate vicinity of the rupture tip; they do not allow description of the stress changes $\Delta\sigma_{ij}$ on the scale of those processes. The nonsingular slip-weakening model introduced by *Ida* [1972] and *Palmer and Rice* [1973], in analogy to cohesive models of tensile cracks by *Barenblatt* [1962] and *Dugdale* [1960], does allow such a description. In that model the fault shear stress τ (= σ_{yx} in mode II, σ_{yz} in mode III) is assumed to undergo a weakening process which begins when τ first reaches a finite peak strength τ_p on an as yet unslipped part of the fault, and then as slip δ begins, τ decreases with δ, approaching a residual strength τ_r at sufficiently large δ. That results in a variation of τ with position x along the fault somewhat like what we show in Figure 8 (although, in general, τ will not vary linearly with x as shown there). We will link τ_p and τ_r to the fault-normal compressive stress $-\sigma^o_{yy}$ by writing

$$\tau_p = (-\sigma^o_{yy}) \tan \phi_p, \quad \tau_r = (-\sigma^o_{yy}) \tan \phi_r.$$

Here $\tan \phi_p$ is the friction coefficient for onset of rapid sliding on the fault, and we set it to 0.577 ($\phi_p = 30°$) in subsequent numerical illustrations. It is less clear what to take for $\tan \phi_r$, or how reasonable it is to regard it as actually constant at large earthquake slip, especially when the possibility of thermal weakening and fluidization of the rapidly shearing fault zone is considered. We will show results for relatively high and low values of $\tau_r/\tau_p = \tan \phi_r/\tan \phi_p$ (0.8 and 0.2, respectively).

[27] The stress distribution near the tip is not readily tractable unless one makes simplifying assumptions about the relation between τ and δ. To approximately determine the stress and express the length R of the slip-weakening zone in terms of properties of the slip-weakening relation, *Palmer and Rice* [1973] adopted the relation which would result in a linear variation of τ with x along the slip-weakening zone (Figure 8),

$$\tau = \begin{cases} \tau_r + (1 + x/R)(\tau_p - \tau_r), & -R < x < 0 \\ \tau_r, & x < -R. \end{cases}$$

A unique slip-weakening relation corresponds to that (it is shown by *Palmer and Rice* [1973] and *Rice* [1980]) and the length R can then be expressed in terms of the fracture energy G. At least that is so in their asymptotic limit case, which we consider too, when R is much less than other length dimensions like overall slipping zone length L. In that limit case, the stress drop $\Delta\tau = \sigma^o_{yx} - \tau_r$ is assumed to be much less than the strength drop $\tau_p - \tau_r$. That was studied for quasi-static rupture growth by Palmer and Rice. *Rice* [1980] pointed out that the solution for dynamic rupture propagation, for the same slip-weakening law, would be provided if R was made a certain function of rupture velocity, which diminished with velocity in a particular way. That is

$$R = \frac{R_0}{f_{\mathrm{II}}(v_r)},$$

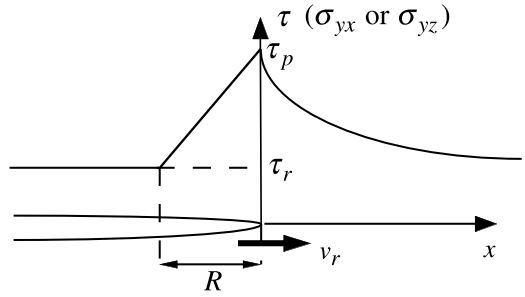

Figure 8. Nonsingular slip-weakening rupture model with linear variation of shear stress (from peak strength τ_p to residual strength τ_r) with the spatial coordinate along the slip-weakening zone. Used to estimate regions of off-plane inelastic response.

where

$$R_0 = \frac{9\pi}{16(1-\nu)} \frac{\mu G}{(\tau_p - \tau_r)^2}$$

for mode II rupture, and

$$R = \frac{R_0}{f_{\mathrm{III}}(v_r)},$$

where

$$R_0 = \frac{9\pi}{16} \frac{\mu G}{(\tau_p - \tau_r)^2}$$

for mode III, where the functions $f(v_r)$ are

$$f_{\mathrm{II}}(v_r) = \frac{\alpha_s(1-\alpha_s^2)}{(1-\nu)[4\alpha_d\alpha_s - (1+\alpha_s^2)^2]}, \quad f_{\mathrm{III}}(v_r) = \frac{1}{\alpha_s},$$

where $\sqrt{1 - v_r^2/c_d^2}$, $\alpha_s = \sqrt{1 - v_r^2/c_s^2}$ and c_d and c_s are the dilational and shear wave speeds. Both of the functions $f(v_r) = 1$ when $v_r = 0^+$, but they increase with v_r (so that the slip-weakening zone contracts in length), without limit as $v_r \to c_{\mathrm{lim}}$. We follow an earlier study by *Rubin and Parker* [1994] in applying that dynamic near tip solution to study off-fault stressing. Previously, *Andrews* [1976a] showed for a mode III slip-weakening model that the predicted maximum shear stress magnitude off the fault plane grows without limit as $v_r \to c_s$, and *Rice* [1980] showed that the average fault-parallel stress alterations predicted along the walls of the slip-weakening zone, i.e., $\Delta\sigma_{xx}$ for mode II and $\Delta\sigma_{xz}$ for mode III, are proportional to $f_{\mathrm{II}}(v_r)$ and $f_{\mathrm{III}}(v_r)$, respectively, times $\tau_p - \tau_r$, and become indefinitely large as $v_r \to c_{\mathrm{lim}}$.

[28] Essentially, in the above expressions, the size R is obtained from the condition that the net stress singularity at the crack tip is zero, due to the K_{II} or K_{III} of the singular crack model being balanced by the intensity factor due to the shear stress excess $\tau - \tau_r$ which provides resistance to displacements in the slip-weakening zone, equations (A12a) and (A12b). That gives

$$K_{\mathrm{II,III}} - \frac{4}{3}(\tau_p - \tau_r)\sqrt{\frac{2}{\pi} R_{\mathrm{II,III}}} = 0,$$

and the result for $R_{II,III}$ is then expressed in terms of G by using [e.g., *Rice*, 1980]

$$G = \frac{1-\nu}{2\mu} f_{II}(v_r) K_{II}^2,$$

or

$$G = \frac{1}{2\mu} f_{III}(v_r) K_{III}^2.$$

The invariant slip-weakening relation between $\tau - \tau_r$ and δ, consistent with any specified value of G, is then obtained by solving for the displacement field under the loading as in Figure 8. The values for the fracture energy G for natural earthquakes vary greatly depending on the method of calculation. *Rice* [2000] used parameters reported for seven large earthquake by *Heaton* [1990], interpreting them with use of a self-healing crack model by *Freund* [1979], to infer average G values for the individual events which range from 0.5 to 5 MJ/m^2.

[29] It is reasonable to assume, at least as an end-member case, that everywhere except at some places of locally high shear stress or low effective normal stress, where earthquakes can readily nucleate, the shear prestress in the crust along major faults is much less than the stress τ_p to initiate slip. Assuming that τ_p is related to the fault-normal precompression like in laboratory and borehole studies, and that the fault-normal stress is comparable to the overburden, we expect τ_p to generally be of the order of 100 MPa at crustal seismogenic depths. On the other hand, to meet heat flow constraints, one is driven to assume that $\tau_r < 10$ MPa to sustain slip during major ruptures. Thus $\tau_p - \tau_r$ would be of the order 100 MPa. That is much larger than a typical seismic stress drop $\Delta\tau$, inferred to be just a few megapascals. That scenario with large $\tau_p - \tau_r$ describes what has been called a ''strong but brittle'' fault [*Rice*, 1996]; ''strong'' because of the high τ_p but ''brittle'' because of the low τ_r. Assuming that abundant regions are present where the effective stress is locally low enough to allow nucleation (say, due to locally low normal stress from nonplanarity of the fault surfaces, or to local pore pressure elevation), models of such strong but brittle faults can allow fault operation at low overall driving stress, and low heat generation, while still agreeing with laboratory friction estimates of strength at the onset of slip [*Rice*, 1996]. Slip-weakening models of that type, with $\Delta\tau \ll \tau_p - \tau_r$ and, correspondingly, R_0 much smaller than any macroscopic length scale like length of the rupture, pose a great challenge for numerical simulations, because they require extreme grid refinement. At least partly for that reason, cases with $\tau_p - \tau_r$ only modestly greater than $\Delta\tau$ are most commonly presented [e.g., *Andrews*, 1976b; *Aochi et al.*, 2002].

[30] Assuming that $\tau_p - \tau_r$ is indeed of order 100 MPa, and using the estimates of G cited above, we can estimate the low-speed length R_0 of the slip-weakening zone to be in the range 4–40 m. Nevertheless, we will soon argue that the inferred G values may include significant energy dissipation in secondary faulting off the main rupture plane [*Andrews*, 1976a], and thus would not correspond to slip on just a single fault, so that the slip weakening zone size could be less than that estimate. At yet another extreme, if we assumed that $\tau_p - \tau_r$ was not large like in the above discussion, but only modestly greater than typical seismic stress drops, say $\tau_p - \tau_r = 10$–20 MPa, then R_0 would be 20–80 times larger than above.

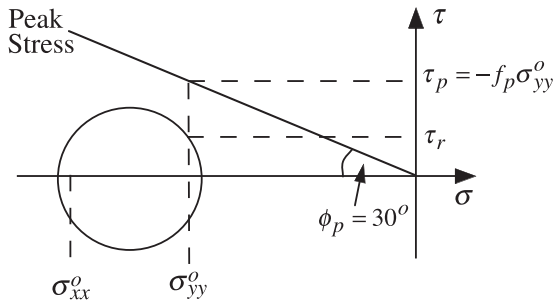

Figure 9. Mohr circle for residual stress field, σ^o_{xx}, σ^o_{yy}, τ_r, along the fault plane far from the tip which, under approximations made, is not very different from that for σ^o_{xx}, σ^o_{yy}, σ^o_{yx}.

3.1. Mode II

[31] Consider a mode II crack tip with the slip-weakening zone moving in the far-field stress σ^o_{xx}, σ^o_{yy}, σ^o_{yx}. The system of coordinates x,y moves with the crack tip at velocity v_r. Writing the stress field as $\sigma_{ij} = \sigma^o_{ij} + \Delta\sigma_{ij}$, the solution for the $\Delta\sigma_{ij}$ is given by equations (A3) in terms of a complex function defined by equation (A11). That solution treats the slipping zone as if it extended semi-infinitely to $x = -\infty$ on a fault in a full space, with a stress drop that is a negligible fraction of the strength drop ($\sigma^o_{yx} - \tau_r \ll \tau_p - \tau_r$). At that level of approximation, we do not distinguish between σ^o_{yx} and τ_r. That simple slip-weakening model is therefore sensible for a strong but brittle fault operating at low overall driving stress, as in the discussion above, but not for a fault with a seismic stress drop that is a significant fraction of $\tau_p - \tau_r$.

3.1.1. Parameterization of the Model

[32] The stresses depend only on the nondimensional velocity v_r/c_s if the Poisson ratio ν is fixed. We have chosen $\nu = 0.25$ ($c_d/c_s = \sqrt{3}$, $c_R/c_s = 0.9194$). The rest of the parameters, namely, initial normal stresses σ^o_{xx}, σ^o_{yy}, as well as peak τ_p and residual τ_r stresses are shown in Figure 9. We choose τ_r/τ_p, $\sigma^o_{xx}/\sigma^o_{yy}$, and v_r/c_s to parameterize. However, there is a limitation on the choice of $\sigma^o_{xx}/\sigma^o_{yy}$ for given τ_r/τ_p if we impose the condition that the residual stress state far behind the rupture tip must cause a maximum shear stress $\tau_{max} = \sqrt{(\sigma^o_{xx} - \sigma^o_{yy})^2/4 + \tau_r^2}$ in the material adjoining the fault which is lower than the Coulomb critical stress of $-(\sigma^o_{xx} + \sigma^o_{yy})\sin(\phi_p)/2$. This condition gives the limits

$$(\sigma^o_{xx}/\sigma^o_{yy})_{min,max} = \left[1 + \sin^2\phi_p \pm 2\sin\phi_p\sqrt{1 - (\tau_r/\tau_p)^2}\right]/\cos^2\phi_p,$$

which reduce when $\phi_p = 30°$ to

$$(\sigma^o_{xx}/\sigma^o_{yy})_{min,max} = (5/3) \pm (4/3)\sqrt{1 - (\tau_r/\tau_p)^2}.$$

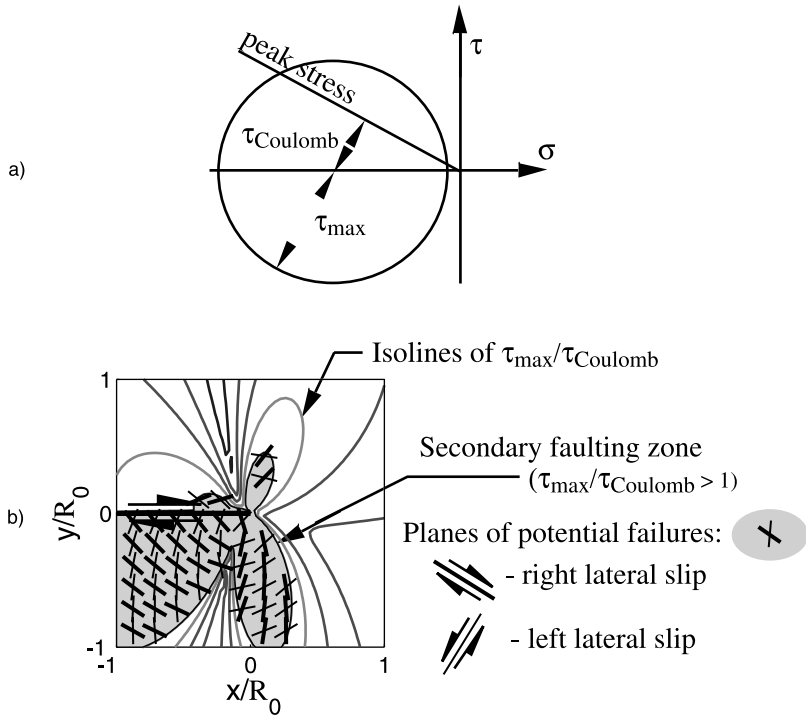

Figure 10. Explanation of mode II plots which follow. (a) Mohr circle representation of maximum shear stress $\tau_{max} = \sqrt{(\sigma_{xx} - \sigma_{yy})^2/4 + \sigma_{xy}^2}$ and the Coulomb limit stress $\tau_{Coulomb} = -(\sigma_{xx} + \sigma_{yy}) \sin(\phi_p)/2$. (b) The $\tau_{max}/\tau_{Coulomb}$ isolines, with coordinates x, y nondimensionalized by the low-speed size R_0 of the slip-weakening zone. The secondary faulting area $\tau_{max}/\tau_{Coulomb} > 1$ is shown in gray.

3.1.2. Explanation of the Figures

[33] Figure 10 explains the notation used in subsequent plots. To demonstrate how close the stress state is to failure,we plot the ratio of maximum shear stress $\tau_{max} = \sqrt{(\sigma_{xx} - \sigma_{yy})^2/4 + \sigma_{xy}^2}$ to the Coulomb limit stress $\tau_{Coulomb} = -(\sigma_{xx} + \sigma_{yy})\sin(\phi_p)/2$ (Figure 10a). Figure 10b is a typical plot of the ratio of $\tau_{max}/\tau_{Coulomb}$ isolines in a box around the tip of a right-lateral shear crack, where the coordinates x,y are nondimensionalized with the low-speed size R_0 of the slip-weakening zone. The activated zone, i.e., where stress is above the peak stress ($\tau_{max}/\tau_{Coulomb} > 1$) is shown in gray. Directions of potential secondary faulting are drawn at the angles $\pm(45^\circ - \phi_p/2) = \pm 30^\circ$ to the most compressive principal stress. These planes are shown by thin solid lines for left-lateral slip and by thick solid lines for right-lateral slip.

3.1.2.1. Influence of Crack Velocity and the Initial Stress

[34] This is shown in Figure 11 for $\tau_r/\tau_p = 0.2$. Isolines of $\tau_{max}/\tau_{Coulomb}$ demonstrate that the stress level and size of the activated zone grow as crack velocity increases. At $v_r/c_s \approx 0.9$ (0.90 corresponds to $v_r/c_R \approx 0.98$) the size of the activated zone becomes comparable to the size of the low-speed slip-weakening zone R_0 or can exceed it, like in the example in Figure 11b for which the size of the secondary faulting zone is around $5R_0$. A perspective on activated zone growth with v_r is as follows: The peak stress τ_p should vary with normal compressive stress $-\sigma_{yy}$, and $\sigma_{yy} = \sigma^o_{yy}$ at all positions along the fault, due to the mode II symmetry. As Figure 12a shows, the shear stress σ_{yx} along the fault plane ahead of the rupture rises to τ_p because of the stress concentration. The Mohr circle for stress states along that plane will, generally, pass outside the Mohr-Coulomb failure envelope at any v_r. Once slip weakening begins, σ_{yx} reduces in size. However, when $v_r \rightarrow c_R$, the size R diminishes toward zero; since the same critical slip-weakening displacement is attained over distance R, that causes strong extensional or compressive straining of the two fault walls [*Rice*, 1980]. The result is very large changes in σ_{xx} along the fault, further driving the stress along the fault itself outside the failure envelope. Much more complex changes in stress state occur off the fault plane.

[35] A striking feature in Figure 11 is that the shape of the activated zone also crucially depends on $\sigma^o_{xx}/\sigma^o_{yy}$. In our discussion of Figures 4 and 5, the qualitative influence of the initial stress ratio on the fracture pattern has already been suggested. When $-\sigma^o_{yy} < -\sigma^o_{xx}$ like in Figure 11a, secondary faulting consistent with branching was predicted to be encouraged on the compressional side, and when $-\sigma^o_{yy} > -\sigma^o_{xx}$ like in Figure 11b, on the extensional. Here we can be more quantitative. The very small angle ψ of the principal stress associated with Figure 11a allows equal activation of secondary faulting on both sides of the rupture. Somewhat larger ψ values, and especially values of $\psi > 45^\circ$ like in Figure 11b, strongly favor secondary faulting on the extensional side.

[36] The mathematical solution shows that σ^o_{xx}, σ^o_{yy} do not change along the fault plane ahead of the rupture tip while the shear stress increases to its peak (Figure 12, insert at the

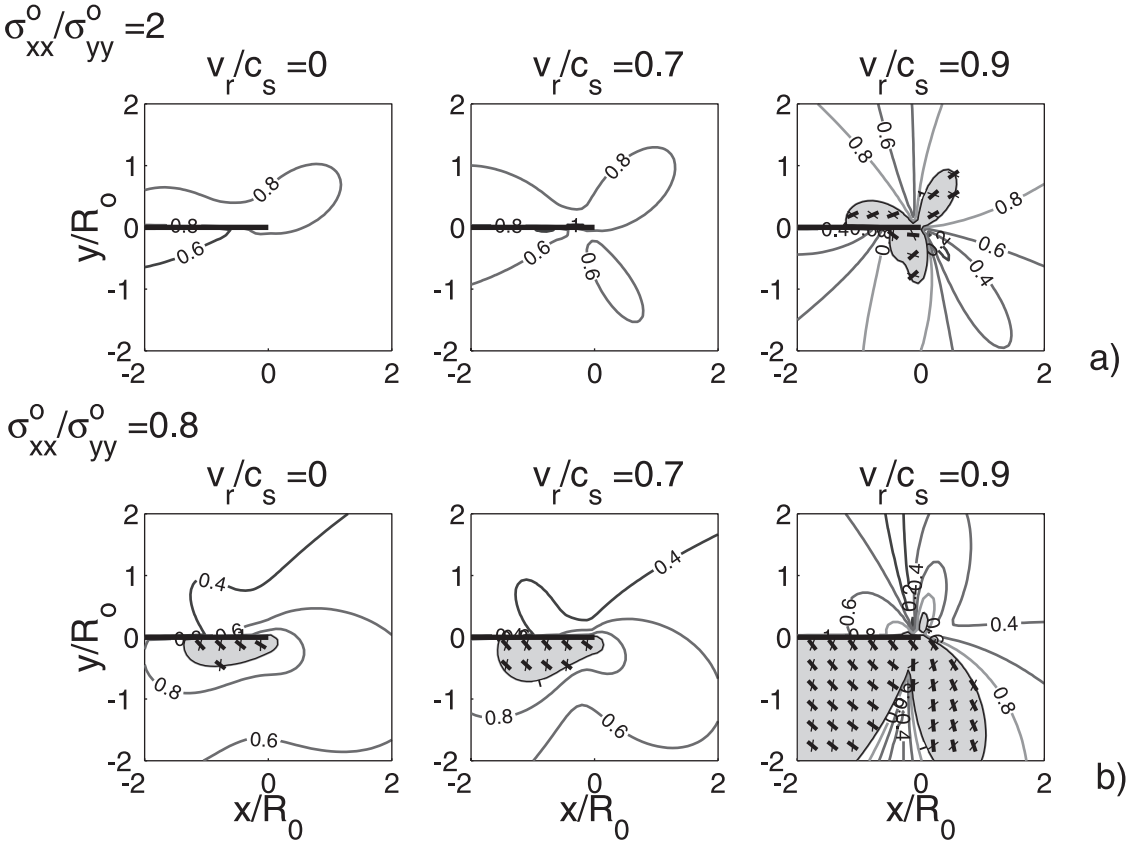

Figure 11. Right-lateral failure with $\tau_p = 0.6(-\sigma^o_{yy})$ and $\tau_r = 0.2\tau_p$ at two prestress ratios and different rupture speeds v_r. Maximum speed shown is 0.90 $c_s \approx 0.98c_R$. (a) The ratio $\sigma^o_{xx}/\sigma^o_{yy} = 2$; $S_{\max}$ angle ψ smaller than 45°, $\psi \approx 7°$ for $\sigma_{yx} = \tau_r \approx \sigma^o_{yx}$, $\psi_p \approx 25°$ for $\sigma_{yx} = \tau_p$. (b) The ratio $\sigma^o_{xx}/\sigma^o_{yy} = 0.8$; $S_{\max}$ angle ψ larger than 45°, $\psi \approx 65°$ for $\sigma_{yx} = \tau_r \approx \sigma^o_{yx}$, $\psi \approx 50°$ for $\sigma_{yx} = \tau_p$.

top). If $\sigma^o_{xx}/\sigma^o_{yy} \approx 1.7$ (for $\phi_p = 30°$) the Coulomb failure condition is achieved only along the fault plane but at no orientations tilting away from it (because the Mohr circle then makes tangential contact with the failure line). If $\sigma^o_{xx}/\sigma^o_{yy} > 1.7$, then for $\sigma_{yx} \rightarrow \tau_p$ ahead of the rupture, surfaces tilting anticlockwise from the main fault plane will be stressed above the Coulomb failure line (Figure 12a). For $\sigma^o_{xx}/\sigma^o_{yy} < 1.7$ the same is true of surfaces tilting clockwise (Figure 12b).

3.1.2.2. Influence of the Residual Strength Ratio τ_r/τ_p

[37] This is shown in Figure 13 for the velocity $v_r/c_s \approx 0.9$. We have chosen $\sigma^o_{xx} = \sigma^o_{yy}$ in order to keep the direction of principal stresses constant (45° with the fault direction) with change of τ_r/τ_p. The size of the activated zone increases with increase of τ_r/τ_p, which can be explained by growth of the shear part of the σ^1_{ij} term. Also, the right-lateral secondary faults are more nearly perpendicular to the main fault for low τ_r/τ_p because the stress field is dominated by the tip stresses, and more nearly parallel to the fault at high τ_r/τ_p because the stress is then controlled by the residual stress τ_r.

3.2. Mode III

[38] For mode III slip weakening, the antiplane shear stresses can be calculated as $\sigma_{yz} = \sigma^o_{yx} + \Delta\sigma_{yz}$, $\sigma_{xz} = \Delta\sigma_{xz}$, with the $\Delta\sigma_{ij}$, given by equations (A6) and (A11), and the assumption is again that $\sigma^o_{yz} - \tau_r \ll \tau_p - \tau_r$. For simplicity, we assume that $\sigma^o_{xx} = \sigma^o_{yy}$ so that τ_p is independent of θ and the solution may be characterized by two nondimensional parameters, v_r/c_s and τ_r/τ_p. To demonstrate how close is the stress to failure, we plot isolines of τ/τ_p, where $\tau = \sqrt{\sigma^2_{yz} + \sigma^2_{xz}}$, as shown in Figure 14. The zone $\tau/\tau_p > 1$ is shown in gray. Directions $\theta_{\max} = \tan^{-1}(-\sigma_{xz}/\sigma_{yz})$ of maximum shear are shown in black. The optimal Coulomb failure planes are not perpendicular to the plane of the diagram, but do intersect along the maximum shear directions shown.

[39] Effects of the crack velocity and residual strength ratio are shown in Figure 15. As in the singular model, the maximum shear stress grows with increasing crack velocity. In this case, τ_r/τ_p appears to be quite important. For $\tau_r/\tau_p = 0.8$ (Figure 15b), the off-fault stress has not attained the peak value τ_p, even at a velocity as high as $v_r/c_s = 0.9$ (but it does at yet higher speed). For $\tau_r/\tau_p = 0.2$ (Figure 15a) the activated zone size reaches the low-speed slip-weakening size R_0 at $v_r/c_s = 0.9$, and forking is likely to occur. In contrast to mode II the shape of the activated zone is symmetric relative to the main fault.

4. Discussion

4.1. Phenomena Related to Fault Dynamics

[40] In this paper we addressed several phenomena related to fault dynamics. These include (1) bending and

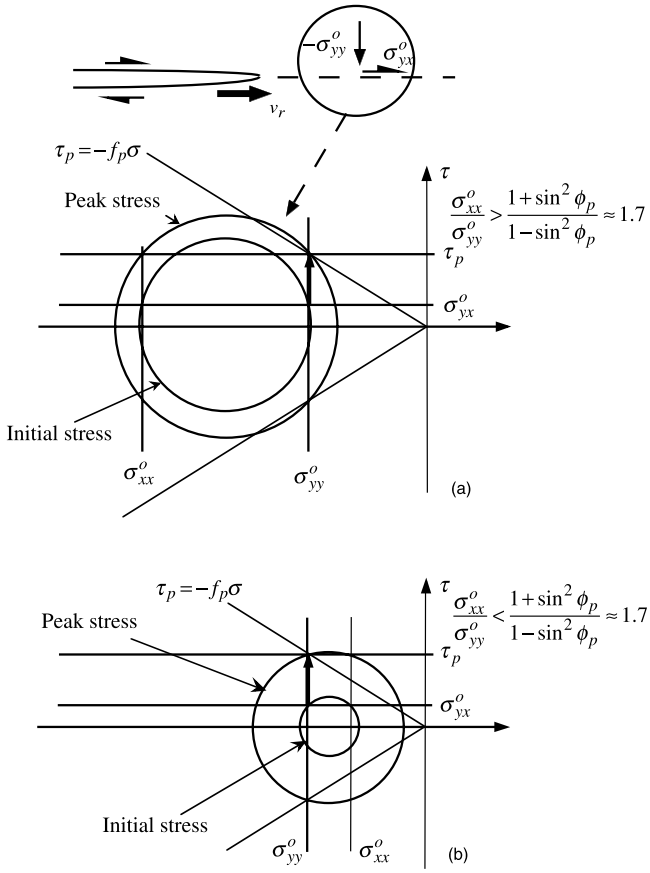

Figure 12. Graphical interpretation of results for different $\sigma^o_{xx}/\sigma^o_{yy}$ in Figure 11. Mohr circle pairs show increase of shear stress $\tau \rightarrow \tau_p$ (following solid arrow) along the fault plane in front of the crack tip (insert on the top explains the location). Substantial increases or decreases (depending on side of fault) of σ_{xx} from σ^o_{xx}, but no change of σ_{yy} from σ^o_{yy}, occur along the fault as σ_{yx} reduces from τ_p to τ_r within the slip weakening zone (Figure 8), especially when v_r is near to c_R. Much more complicated changes of the Mohr circles occur off the fault plane. (a) For $\sigma^o_{xx}/\sigma^o_{yy} > 1.7$, surfaces of anticlockwise orientation relative to the main fault plane will be stressed above the Coulomb failure line. (b) For $\sigma^o_{xx}/\sigma^o_{yy} < 1.7$ the same is true of surfaces of clockwise orientation.

bifurcation of the rupture path, (2) intermittency in fracture propagation, (3) high fracture energy observed for natural earthquakes, and (4) activation of secondary faulting regions within damage zones bordering a major fault. These issues are discussed further below.

4.1.1. Crack Acceleration and Dynamic Growth of Off-Plane Stresses at High Velocities

[41] The hypothesis of our work is that the dynamic stress field near the tip of a rapidly propagating rupture plays a major role in all above mentioned phenomena. Theoretical elastodynamic models of nonuniform crack extension [*Kostrov*, 1966, 1975; *Eshelby*, 1969; *Freund*, 1972a, 1972b; *Fossum and Freund*, 1975] have shown that fractures which remain on a plane have a tendency to accelerate to their limiting speed (shear wave speed for mode III and Rayleigh speed for mode II). However, studies of high-speed crack tip stresses (*Yoffe* [1951] for mode I, *Erdogan* [1968] and *Andrews* [1976a] for mode III, B. V. Kostrov (orally reported results, Bad Honnef, Germany, 1978, as cited by *Rice* [1980]), and *Rice* [1980] for mode II) clearly demonstrate that off-fault stresses grow rapidly as the crack speed approaches the limiting speed.

4.1.2. Intermittency of Rupture Propagation

[42] These strong off-fault stresses may cause extensive local failures near the main rupture tip, and may force the rupture to bend or fork at the conditions discussed. However, continued slip on a fault bend may be incompatible with the larger-scale stress field. In such cases, propagating ruptures may be self-destabilizing near the limiting speed. That is, having begun along a path that the larger-scale stress state cannot sustain, they may be subject to arrest or to discontinuous propagation. We think it is likely that shear fault dynamics will ultimately be understood in ways that have recently been quite productive for dynamic tensile (mode I) cracking [e.g., *Rice*, 2001]. In that case, cracks do not reach their theoretical terminal speed c_R because extensive secondary cracking develops off the main crack plane [*Ravi-Chandar and Knauss*, 1984a, 1984b, 1984c; *Sharon et al.*, 1995, 1996]. We have argued here that analogous effects should occur for shear cracks. The effect of further increase in applied force, which would drive v_r, although the local v_r becomes even more highly oscillatory [*Ravi-Chandar and Knauss*, 1984a, 1984b, 1984c; *Sharon et al.*, 1995]. At yet further increase of applied force, macroscale forking of the fracture path occurs. We are suggesting a similar source of highly intermittent rupture propagation in shear, with similar highly oscillatory v_r, that should be a source of enriched high frequency seismic radiation from faults (compared to what one would expect for smooth rupture propagation).

4.1.3. High Values of Fracture Energy

[43] Figures 11, 13, and 15 show the growth of the off-fault region where material undergoes inelastic response as $v_r \rightarrow c_{\lim}$. Like for tensile cracks, and as already suggested by *Andrews* [1976a] for mode III, that seems likely to make the net fracture energy G increase significantly over the part of G ascribable to the slip-weakening process on the main fault plane. This has a potential connection to two important problems: The expected rapid increase of G with increase of v_r, at speeds very near c_R, makes the barrier at c_R harder to pass than for the ordinary slip weakening model [*Andrews*, 1976b; *Burridge et al.*, 1979]. That may help explain why seismic inferences of super-Rayleigh propagation speeds are relatively rare. Also, the very large G values inferred for major earthquakes, typically averaging 0.5 to 5 MJ/m^2 for individual events [e.g., *Rice*, 2000], must be expected to involve significant contributions to the energy dissipation from outside the main fault surface. The same G values would not apply to ruptures moving only modestly slower on the same fault (compare extent of off-fault activity predicted for $v_r = 0.7\ c_s$ with $0.9\ c_s$ in Figures 11 and 15), and neither would they apply to ruptures in the early phases of growth as

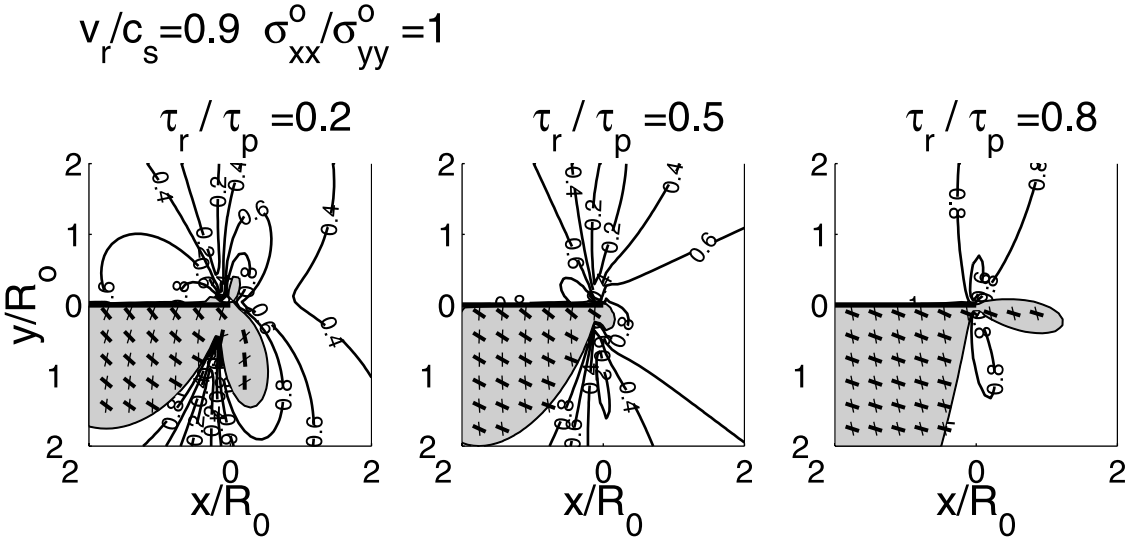

Figure 13. Effect of ratio of residual strength, τ_r, to peak strength, $\tau_p = 0.6(-\sigma^o_{yy})$, shown for a high rupture speed, $v_r/c_s = 0.9$, and for $\sigma^o_{xx}/\sigma^o_{yy} = 1$ (so that $\psi = 45°$).

they are nucleated. So there is no longer necessarily the paradox that the G values are so large that we could not reconcile them with lab values or understand how small earthquakes with only tens of meters overall rupture dimension could occur.

4.1.4. Size of Secondary Faulting Zone

[44] The structure of a mature seismogenic fault is complex. It typically contains a narrow core (less than tens of centimeters thick) where the major part of tectonic slip is accommodated, with the possibility that individual slip events occupy only a few millimeters of width within it [*Chester and Chester*, 1998]. The fault core is bounded by a zone of damaged host rock of the order of 100 m thick [*Chester et al.*, 1993]. Our models do not explain the formation of the whole damage zone, which probably involves the modeling of the history of repeated deformations in shear along fractally mismatched surfaces [*Power et al.*, 1988]. However, our models demonstrate stressing which should activate a secondary faulting zone where $\tau/\tau_p > 1$ (which is shown in gray in Figures 11, 13, and 15). We suggest that during earthquakes some part of the deformation is accommodated in this zone. The predicted size of the activated region strongly depends on all studied parameters. However, the dependence on the velocity of propagation is straightforward: it grows with $v_r/c_{\lim}$ because of the increase of off-fault stresses. For high velocities (i.e., $v_r/c_{\lim} = 0.9$) its size reaches the size of slip-weakening region $\sim R_0$, which was roughly estimated to be 4–40 m, or possibly less depending on how much of the inferred G corresponds to slip weakening on the main fault plane. Thus the estimated size of the zone of secondary faulting is smaller or at most equal to the size of the damage zone.

4.1.5. Influence of the Residual and Initial Stresses

[45] The illustrations in Figure 11 for two ratios of $\sigma^o_{xx}/\sigma^o_{yy}$ hint at the remarkably large effect of that prestress ratio, which is well illustrated in Figures 4 and 5. The case $\sigma^o_{xx}/\sigma^o_{yy} = 2$ in Figure 11a is close to having the fault plane itself be optimally oriented for rupture, in the Mohr-Coulomb sense, when σ_{yx} first reaches τ_p. Comparable regions on both the extensional ($y < 0$) and compressional ($y > 0$) side are then activated. However, laboratory [*Savage et al.*, 1996] and seismicity-based [*Hardebeck and Hauksson*, 1999] inferences suggest that prestress states are closer to the $\sigma^o_{xx}/\sigma^o_{yy} = 1$ case of Figure 13, for which the off-plane activity is very different, and almost completely confined to the extensional side.

4.2. Natural Observations and Comparisons With Theory

[46] Despite the fact that the directions of principal stresses in nature are generally not well constrained we can compare our theoretical results with some natural examples. These are discussed in connection with Figure 16 and are as follows:

[47] 1. The San Fernando 1971 earthquake zone is sketched in Figure 16a following *Heaton and Helmberger* [1979]. It is a reasonable assumption that the maximum

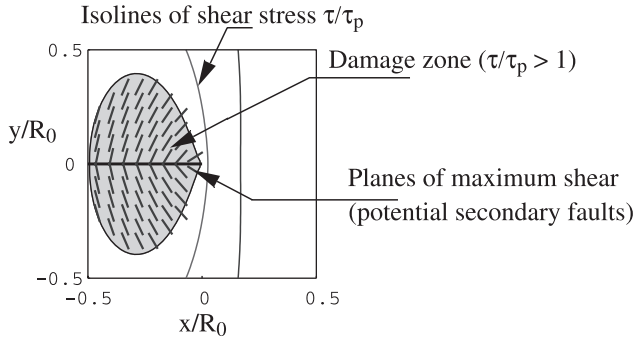

Figure 14. Explanation of mode III plots. The isolines of ratio of $\tau = \sqrt{\sigma^2_{yz} + \sigma^2_{xz}}$ to τ_p are shown to demonstrate the closeness to failure. The ratio $\tau/\tau_p > 1$ in the gray area. Directions $\theta_{\max} = \tan^{-1}(-\sigma_{xz}/\sigma_{yz})$ of maximum shear shown as solid lines.

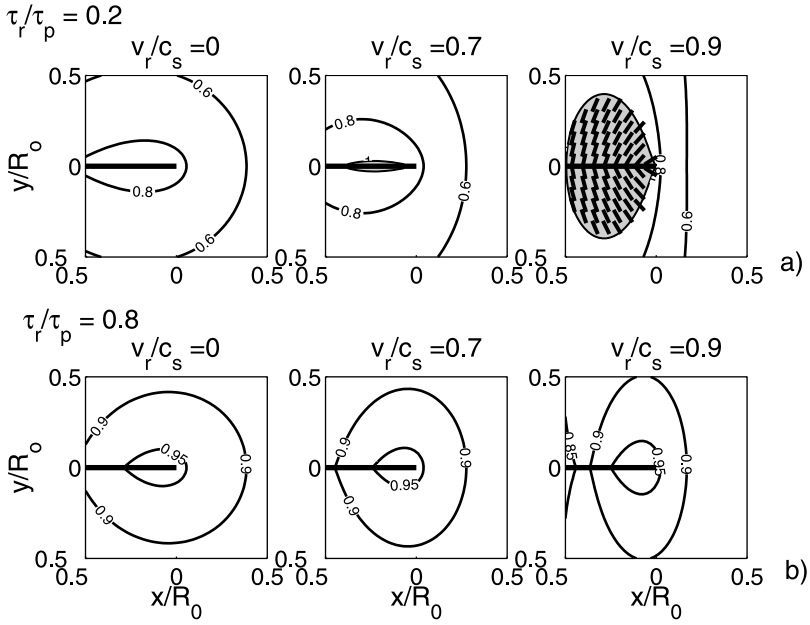

Figure 15. Mode III failure at different rupture speeds v_r, with $\tau_r = 0.2\tau_p$ and $\tau_r = 0.8\tau_p$.

compression is horizontal. Because the earthquake took place on the reverse 53° dip fault, the angle between the maximum compressive stress and main fault (as in the case with Figure 11b) is high. Consistent with our model, the main fault bends (at 24°) to the extensional side.

[48] 2. The Kettleman Hills earthquake (Figure 16b from *Ekstrom et al.* [1992]) took place as a low angle thrust fault and represents an example where most compressive stress makes a low angle to the fault like in Figure 11a. In this case our results suggest a secondary faulting zone on the compressional and extensional side from the main fault which is consistent with the observed aftershock activity, although there is no evidence on whether dynamic branching occurred in this case.

[49] 3. The Landers 1992 earthquake jumped from a main (the Johnson Valley) fault to the Kickapoo, or Landers, fault located on the extensional side (Figure 16c, from *Sowers et al.* [1994]). On the basis of inference of principal stress directions from microseismicity by *Hardebeck and Hauksson* [2001], the principal stress direction near the bifurcation of the rupture path is approximately 30° east of north. On the other hand, the tangent direction to the Johnson Valley fault is about 30° west of north. Thus there is an approximately 60° angle between the most compressive stress and the main fault. This is like the case shown in the Figure 11b, demonstrating extensive above peak stresses on the extensional side, and so the observed branching is consistent with our theoretical concepts.

[50] It is also interesting to compare the presence and geometry of small slip-accumulating faults that curve off the main fault and then stop, as mapped in detail by *Sowers et al.* [1994] along the most northern branch of Johnson Valley fault, and the southern reach of Homestead Valley fault. Both fault segments ruptured in the Landers 1992 earthquake and are almost parallel to each other (see our Figure 16c and, especially, Plate 2 of *Sowers et al.* [1994]). However, the rupture along the most northern branch of the Johnson Valley fault was a right-lateral NNW slip that continued only around 4 km past the junction with the Kickapoo fault, with less and less slip as detailed by *Sowers et al.* [1994]. It had small, also unsuccessful, faults branching off to its eastern, extensional side. By contrast the rupture on the southern reach of Homestead Valley fault, also unsuccessful in itself, was a right-lateral slip that started presumably at the junction with the Kickapoo fault and went SSE, also approximately over a distance around 4 km, with diminishing slip as also detailed by *Sowers et al.* [1994]. It had a pattern of off-branching small faults again to its extensional side, which is then its western side. Thus the pattern of secondary activity along both of these faults is correlated with their rupture directions in the manner that would be expected from our analysis. Such correlations in other cases may be useful for paleoseismological inferences of rupture directivity.

[51] 4. Another branching case is the 1979 Imperial Valley earthquake shown in Figure 16d (our drawing is based on the map of *Archuleta* [1984]). The approximate maximum stress direction is north-south if we judge from the stress directions inferred by *Hardebeck and Hauksson* [1999] along their most southern traverse which passes somewhat to the north-west of the bifurcation. While their results average to north-south, individual estimates vary as much as 14° to the east or west of north. That average principal direction would be at approximately 35° to the main fault. The angle is steep enough for the main off-fault activity to take place on the extensional side, as found in simulations of cases which we did not show here. So once again the branching seems interpretable in terms of the concepts developed.

Appendix A: Stresses Near a Propagating Shear Rupture

[52] We consider the two-dimensional plane strain and/or antiplane strain problem of a shear rupture moving with velocity v_r in an elastic material (Figures 1, 6, and 8), and

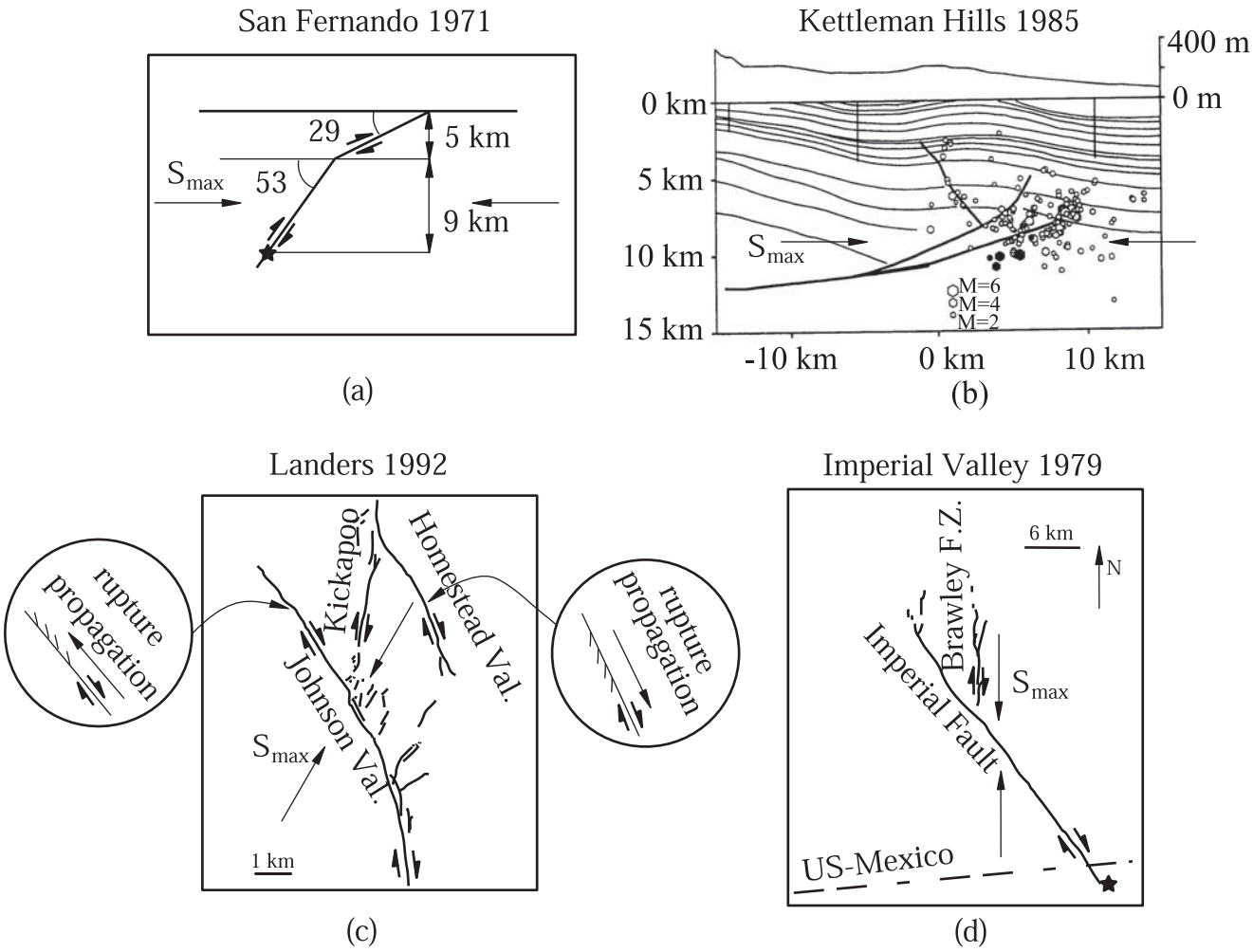

Figure 16. Natural fault systems exhibiting off-main-fault activity. (a) San Fernando 1971 earthquake. The maximum compressive stress, if horizontal, makes a 53° angle with the main fault [*Heaton and Helmberger*, 1979]. The fault bends to the extensional side consistent with our model. (b) Kettleman Hills 1985 earthquake [*Ekstrom et al.*, 1992]. The most compressive stress makes a low angle ($\leq 20°$) with the main thrust fault. Aftershock activity takes place on the extensional and compressional sides as suggested in Figure 11a. (c) Johnson Valley 1992 rupture, at start of the Landers 1992 earthquake, bending along the Kickapoo (or Landers) fault zone [*Sowers et al.*, 1994]. (d) Imperial Valley 1979 rupture bending onto the Brawley fault zone [*Archuleta*, 1984].

assume that in the vicinity of the rupture tip the field is steady in the sense that it depends only on $x - v_r t$ and y. Following the analysis of *Kostrov and Nikitin* [1970], also reviewed by *Rice* [1980] and *Dmowska and Rice* [1986], the elastodynamic equations have subsonic solutions in the form

$$\begin{aligned} u_x &= \mathrm{Re}[F(z_d) + G(z_s)], \\ u_y &= \mathrm{Re}[i\alpha_d F(z_d) + (i/\alpha_s) G(z_s)], \\ u_z &= \mathrm{Re}[H(z_s)]. \end{aligned} \tag{A1}$$

Here F, G, and H are analytic functions of the complex variables indicated, defined by $z_d = x + i\alpha_d y$ and $z_s = x + i\alpha_s y$, where $\alpha_d = \sqrt{1 - v_r^2/c_d^2}$, $\alpha_s = \sqrt{1 - v_r^2/c_s^2}$, and c_d and c_s are dilatational and shear wave speeds, and Re means the real part.

[53] Using equation (A1) in the isotropic elastic stress strain relations, the stress alterations $\Delta\sigma_{\alpha\beta}$ from the uniform prestress state $\sigma^o_{\alpha\beta}$ are then

$$\begin{aligned} \Delta\sigma_{xx} &= \mu\,\mathrm{Re}[(1 - \alpha_s^2 + 2\alpha_d^2)F'(z_d) + 2G'(z_s)], \\ \Delta\sigma_{yy} &= \mu\,\mathrm{Re}[-(1 + \alpha_s^2)F'(z_d) - 2G'(z_s)], \\ \Delta\sigma_{yx} &= \mu\,\mathrm{Im}[2\alpha_d F'(z_d) + ((1 + \alpha_s^2)/\alpha_s)G'(z_s)], \\ \Delta\sigma_{xz} - i\Delta\sigma_{yz}/\alpha_s &= \mu H'(z_s), \end{aligned} \tag{A2}$$

and $\Delta\sigma_{zz} = \nu(\Delta\sigma_{xx} + \Delta\sigma_{yy})$, where ν is the Poisson ratio.

[54] In order to find the relation between the F and G functions, note that antisymmetry and linearity require that the normal stress alteration $\Delta\sigma_{yy} = 0$ on $y = 0$. Because, $z_s = z_d = x$ on $y = 0$, that means $G'(z) = -(1 + \alpha_s^2)F'(z)/2$ on the real z axis, a relation which must also be satisfied at $z = \infty$. It then follows from the theory of analytic functions that the relation is true everywhere. Defining a new analytic func-

tion $M(z) = (i\mu D/2\alpha_s)F'(z)$, where $D = 4\alpha_s\alpha_d - (1 + \alpha_s^2)^2$ is the Rayleigh function, the alteration $\Delta\sigma_{yx}$ of the in-plane shear component of stress along the x axis is given as $\Delta\sigma_{yx}(x,y = 0) = \mathrm{Re}[M(x)]$, and the alterations of the in-plane stresses at general locations are

$$\begin{aligned}\Delta\sigma_{xx} &= 2\alpha_s\,\mathrm{Im}[(1 - \alpha_s^2 + 2\alpha_d^2)M(z_d) - (1 + \alpha_s^2)M(z_s)]/D,\\ \Delta\sigma_{yy} &= -2\alpha_s(1 + \alpha_s^2)\mathrm{Im}[M(z_d) - M(z_s)]/D,\\ \Delta\sigma_{yx} &= -\mathrm{Re}[4\alpha_s\alpha_d M(z_d) - (1 + \alpha_s^2)^2 M(z_s)]/D.\end{aligned} \tag{A3}$$

An appropriate analytic function for the singular crack tip solution [e.g., *Kostrov and Nikitin*, 1970; *Freund*, 1990], also including the only nonsingular term of the stress alteration which is nonzero at the tip, is

$$M(z) = \frac{K_{\mathrm{II}}}{\sqrt{2\pi}} z^{-1/2} - \Delta\tau = \frac{K_{\mathrm{II}}}{\sqrt{2\pi\rho}} e^{-i\phi/2} - \Delta\tau. \tag{A4}$$

Here $\rho = (x^2 + \alpha^2 y^2)^{1/2} = r(\cos^2\theta + \alpha^2 \sin^2\theta)^{1\backslash 2}$ and $\phi = \tan^{-1}(\alpha y/x) = \tan^{-1}(\alpha \tan\theta)$, where the variables α, ρ, ϕ will have either d or s as subscript, K_{II} is the mode II stress intensity factor, and $\Delta\tau = \sigma_{yx}^{o} - \tau_r$ is the stress drop on the rupture. Finally, the crack tip stress alterations are

$$\begin{aligned}\Delta\sigma_{xx} &= -\frac{K_{\mathrm{II}}}{\sqrt{2\pi}}\left[\frac{2\alpha_s(1 - \alpha_s^2 + 2\alpha_d^2)}{D}\frac{\sin(\phi_d/2)}{\sqrt{\rho_d}} - \frac{2\alpha_s(1 + \alpha_s^2)}{D}\frac{\sin(\phi_s/2)}{\sqrt{\rho_s}}\right],\\ \Delta\sigma_{yy} &= \frac{K_{\mathrm{II}}}{\sqrt{2\pi}}\frac{2\alpha_s(1 + \alpha_s^2)}{D}\left[\frac{\sin(\phi_d/2)}{\sqrt{\rho_d}} - \frac{\sin(\phi_s/2)}{\sqrt{\rho_s}}\right],\\ \Delta\sigma_{yx} &= \frac{K_{\mathrm{II}}}{\sqrt{2\pi}}\left[\frac{4\alpha_s\alpha_d}{D}\frac{\cos(\phi_d/2)}{\sqrt{\rho_d}} - \frac{(1 + \alpha_s^2)^2}{D}\frac{\cos(\phi_s/2)}{\sqrt{\rho_s}}\right] - \Delta\tau.\end{aligned} \tag{A5}$$

The singular $(1/\sqrt{r})$ part of this was used for the plots in Figures 2 and 3.

[55] For antiplane strain we can put the equations in an analogous form by defining $M(z) = i\mu\alpha_s H'(z)$, so that the antiplane shear stress alteration $\Delta\sigma_{yz}$ along the x axis is $\Delta\sigma_{yz}(x,y = 0) = \mathrm{Re}[M(x)]$ and the full field is

$$\Delta\sigma_{yz} = \mathrm{Re}[M(z_s)],\ \Delta\sigma_{xz} = \mathrm{Im}[M(z_s)/\alpha_s]. \tag{A6}$$

The analogous singular crack tip solution, again including also the only nonsingular term of the stress alteration which is nonzero at the tip, is

$$M(z) = \frac{K_{\mathrm{III}}}{\sqrt{2\pi}} z^{-1/2} - \Delta\tau = \frac{K_{\mathrm{III}}}{\sqrt{2\pi\rho}} e^{-i\phi/2} - \Delta\tau, \tag{A7}$$

where now K_{III} is the mode III stress intensity factor and the stress drop term is $\Delta\tau = \sigma_{yz}^{o} - \tau_r$. In this case the crack tip stress alterations are

$$\Delta\sigma_{xz} = \frac{K_{\mathrm{III}}}{\alpha_s\sqrt{2\pi\rho_s}}\sin(\phi_s/2), \quad \Delta\sigma_{yz} = \frac{K_{\mathrm{III}}}{\sqrt{2\pi\rho_s}}\cos(\phi_s/2) - \Delta\tau. \tag{A8}$$

In order to minimize the number of parameters in this first study, the slip weakening analysis has been done for the case in which the size R of the slip-weakening zone is negligibly small compared to the overall slipping length of the fault. That corresponds to the case in which the stress drop $\Delta\tau$ is a negligible fraction of the strength drop $\tau_p - \tau_r$. At this level of approximation, we do not distinguish between τ_r and σ_{yx}^{o} or between τ_r and σ_{yz}^{o}. In general, the distribution of shear stress τ (= σ_{yx} for in-plane, σ_{yz} for antiplane; Figure 8) with position x along the rupture must be determined by specifying a constitutive relation, $\tau = \tau(\delta)$, between τ and the slip δ. However, we follow the simpler procedure of *Palmer and Rice* [1973] and *Rice* [1980] in assuming a simple linear distribution of τ with position (Figure 8), and accept whatever $\tau(\delta)$ relation which results, choosing R to be consistent with a given fracture energy G related to it by [*Palmer and Rice*, 1973]

$$G = \int_0^\infty [\tau(\delta) - \tau_r]d\delta. \tag{A9}$$

The external loading, characterized by K_{II} or K_{III}, must be consistent with that G and the net singularity of stress must be removed at the tip. *Palmer and Rice* [1973] did that in the quasi-static situation ($v_r = 0^+$), in which case we denote R as R_0, and showed that a plausible form of slip weakening relation, $\tau = \tau(\delta)$, resulted. *Rice* [1980] then showed that the solution could be obtained for the dynamic case, of interest here, in a way which satisfied that same $\tau = \tau(\delta)$ if R was related to R_0, and hence to G and $\tau_p - \tau_r$, in a specific, speed-dependent manner as described in the text.

[56] Thus to develop a solution, remembering that we do not distinguish between τ_r and σ_{yx}^{o} (or σ_{yz}^{o}) at this level of approximation, we wish to find an analytic function $M(z)$ that is cut along $-\infty < x < 0$, which satisfies

$$\mathrm{Re}[M(x)] = \begin{cases} 0, & -\infty < x < -R \\ (1 + x/R)(\tau_p - \tau_r), & -R < x < 0 \end{cases} \tag{A10}$$

(since the shear stress alteration must equal $\mathrm{Re}[M(x)]$), satisfies $M(z) \approx K/\sqrt{2\pi z}$ as $|z| \to \infty$ (where K denotes K_{II} or K_{III}), and is nonsingular at $z = 0$. The solution, corresponding to that of *Palmer and Rice* [1973] and *Rice* [1980], is

$$M(z) = \frac{2}{\pi}(\tau_p - \tau_r)\left[\left(1 + \frac{z}{R}\right)\tan^{-1}\left(\frac{z}{R}\right)^{-1/2} - \left(\frac{z}{R}\right)^{1/2}\right], \tag{A11}$$

where

$$K - \frac{4}{3}(\tau_p - \tau_r)\sqrt{\frac{2}{\pi}R} = 0 \tag{A12a}$$

or

$$R = 9\pi K^2/32(\tau_p - \tau_r)^2 \tag{A12b}$$

to remove the singularity. This solution is further expressed in terms of rupture speed v_r, fracture energy G, and strength drop $\tau_p - \tau_r$ as described in the text.

[57] **Acknowledgments.** The work was supported at Harvard University by a subcontract from the Southern California Earthquake Center (this is SCEC contribution 607), funded by NSF Cooperative Agreement EAR-8920136 and USGS Cooperative Agreements 14-08-0001-A0899 and 1434-HQ-97AG01718, and also in early phases of the study by USGS

grant 99-HQ-GR-0025, and later by NSF EAR grant 0105344. A visit to Harvard by A.N.B.P. for participation was supported by a NATO Fellowship through the Conservatoire National des Arts et Metiers (code 2300FR) and by French CNRS funding. We are grateful for review comments which improved the manuscript by Allan Rubin of Princeton and D. Joseph Andrews of USGS. We thank David D. Oglesby of UC Riverside and John E. Shaw of Harvard for discussions of thrust fault branching and Robert Parsons of Harvard for checking some of the calculations.

References

Andrews, D. J., Rupture propagation with finite stress in antiplane strain, *J. Geophys. Res.*, *81*, 3575–3582, 1976a.

Andrews, D. J., Rupture velocity of plane strain shear cracks, *J. Geophys. Res.*, *81*, 5679–5687, 1976b.

Aochi, H., and E. Fukuyama, Three-dimensional nonplanar simulation of the 1992 Landers earthquake, *J. Geophys. Res.*, *107*(B2), 2035, doi:10.1029/2000JB000061, 2002.

Aochi, H., E. Fukuyama, and M. Matsu'ura, Spontaneous rupture propagation on a non-planar fault in 3D elastic medium, *Pure Appl. Geophys.*, *157*(11/12), 2003–2027, 2000a.

Aochi, H., E. Fukuyama, and M. Matsu'ura, Selectivity of spontaneous rupture propagation on a branched fault, *Geophys. Res. Lett.*, *27*, 3635–3638, 2000b.

Aochi, H., R. Madariaga, and E. Fukuyama, Effect of normal stress during rupture propagation along nonplanar faults, *J. Geophys. Res.*, *107*(B2), 2038, 10.1029/2001JB000500, 2002.

Archuleta, R. J., A faulting model for the 1979 Imperial Valley earthquake, *J. Geophys. Res.*, *89*, 4559–4585, 1984.

Aydin, A., and R. A. Schultz, Effect of mechanical interaction on the development of strike-slip faults with echelon patterns, *J. Struct. Geol.*, *12*, 123–129, 1990.

Barenblatt, G. I., The mathematical theory of equilibrium cracks in brittle fracture, *Adv. Appl. Mech.*, *7*, 55–80, 1962.

Barka, A., and K. Kadinsky-Cade, Strike-slip fault geometry in Turkey and its influence on earthquake activity, *Tectonics*, *7*, 663–684, 1988.

Bouchon, M., and D. Streiff, Propagation of a shear crack on a nonplanar fault: A method of calculation, *Bull. Seismol. Soc. Am.*, *87*, 61–66, 1997.

Burridge, R., G. Conn, and L. B. Freund, The instability of a rapid mode II shear crack with finite cohesive traction, *J. Geophys. Res.*, *84*, 2210–2222, 1979.

Buwalda, J. P., and P. St. Amand, Geological effects of the Arvin-Tehachapi earthquake, in *Earthquakes in Kern County, California During 1952*, edited by G. B. Oakeshott, *Bull. Div. Mines Geol.*, *171*, 41–56, 1955.

Camacho, G. T., and M. Ortiz, Computational modelling of impact damage in brittle materials, *Int. J. Solids Struct.*, *33*, 2899–2938, 1996.

Chester, F. M., and J. S. Chester, Ultracataclasite structure and friction processes of the Punchbowl Fault, San Andreas system, California, *Tectonophysics*, *295*(1–2), 199–221, 1998.

Chester, F. M., J. P. Evans, and R. L. Biegel, Internal structure and weakening mechanisms of the San Andreas fault, *J. Geophys. Res.*, *98*, 771–786, 1993.

Cocco, M., and J. R. Rice, Pore pressure and poroelasticity effects in Coulomb stress analysis of earthquake interactions, *J. Geophys. Res.*, *107*(B2), 2030, 10.1029/2000JB000138, 2002.

Dmowska, R., and J. R. Rice, Fracture theory and its seismological application, in *Continuum Theories in Solid Earth Physics, Phys. Evol. Earth's Inter.*, vol. 3, edited by R. Teisseyre, pp. 187–255, Elsevier Sci., New York, 1986.

Dugdale, D. S., Yielding of steel sheets containing slits, *J. Mech. Phys. Solids*, *8*, 100–115, 1960.

Eaton, J. P., The earthquake aftershocks from May 2 through September 30, 1983, in *The Coalinga, California, Earthquake of May 2, 1983*, edited by M. J. Rymer and W. L. Ellsworth, *U.S. Geol. Surv. Prof. Pap.,1487*, 113–170, 1990.

Ekstrom, G., R. S. Stein, J. P. Eaton, and D. Eberhart-Phillips, Seismicity and geometry of a 110-km-long blind thrust fault, 1, The 1985 Kettleman Hills, California, earthquake, *J. Geophys. Res.*, *97*, 4843–4864, 1992.

Erdogan, F., Crack propagation theories, in *Fracture: An Advanced Treatise, Math. Fundam.*, vol. 2, edited by H. Liebowitz, pp. 497–590, Academic, San Diego, Calif., 1968.

Eshelby, J. D., The elastic field of a crack extending non-uniformly under general anti-plane loading, *J. Mech. Phys. Solids*, *17*, 177–199, 1969.

Falk, M. L., A. Needleman, and J. R. Rice, A critical evaluation of cohesive zone laws in dynamic fracture simulations, *J. Phys. IV*, *11*, Pr5-43-52, 2001.

Fossum, A. F., and L. B. Freund, Nonuniformly moving shear crack model of a shallow focus earthquake mechanism, *J. Geophys. Res.*, *80*, 3343–3347, 1975.

Freund, L. B., Crack propagation in an elastic solid subject to general loading, I, Constant rate of extension, *J. Mech. Phys. Solids*, *20*, 129–140, 1972a.

Freund, L. B., Crack propagation in an elastic solid subject to general loading, II, Non-uniform rate of extension, *J. Mech. Phys. Solids*, *20*, 141–152, 1972b.

Freund, L. B., The mechanics of dynamic shear crack propagation, *J. Geophys. Res.*, *84*, 2199–2209, 1979.

Freund, L. B., *Dynamic Fracture Mechanics*, Cambridge Univ. Press, Cambridge, U.K., 1990.

Gordon, F. R., and J. D. Lewis, The Meckering and Calingiri earthquakes October 1968 and March 1970, *Geol. Surv. West. Aust. Bull.*, *126*, 229 pp., 1980.

Hardebeck, J. L., and E. Hauksson, Role of fluids in faulting inferred from stress field signatures, *Science*, *285*, 236–239, 1999.

Hardebeck, J. L., and E. Hauksson, Crustal stress field in southern California and its implications for fault mechanics, *J. Geophys. Res.*, *106*, 21,859–21,882, 2001.

Harris, R. A., and S. M. Day, Dynamics of fault interaction: parallel strike-slip faults, *J. Geophys. Res.*, *98*, 4461–4472, 1993.

Harris, R. A., and S. M. Day, Dynamic 3D simulations of earthquakes on en echelon faults, *Geophys. Res. Lett.*, *26*, 2089–2092, 1999.

Harris, R. A., R. J. Archuleta, and S. M. Day, Fault steps and the dynamic rupture process: 2-d numerical simulations of a spontaneusly propagating shear fracture, *Geophys. Res. Lett.*, *18*, 893–896, 1991.

Harris, R. A., J. F. Dolan, R. Hartleb, and S. M. Day, The 1999 Izmit, Turkey, earthquake: A 3D dynamic stress transfer model of intraearthquake triggering, *Bull. Seismol. Soc. Am.*, *92*, 245–255, 2002.

Hauksson, E., L. M. Jones, and K. Hutton, The 1994 Northridge earthquake sequence in California: Seismological and tectonic aspects, *J. Geophys. Res.*, *100*, 12,335–12,356, 1995.

Heaton, T. H., Evidence for and implications of self-healing pulses of slip in earthquake rupture, *Phys. Earth Planet. Inter.*, *64*, 1–20, 1990.

Heaton, T. H., and D. V. Helmberger, Generalized ray models of the San-Fernando earthquake, *Bull. Seismol. Soc. Am.*, *69*, 1311–1341, 1979.

Ida, Y., Cohesive force across the tip of a longitudinal shear crack and Grifith's crack specific surface energy, *J. Geophys. Res.*, *77*, 3796–3805, 1972.

Johnson, E., Process region changes for rapidly propagating cracks, *Int. J. Fract.*, *55*, 47–63, 1992.

Kame, N., and T. Yamashita, Dynamic nucleation process of shallow earthquake faulting in a fault zone, *Geophys. J. Int.*, *128*, 204–216, 1997.

Kame, N., and T. Yamashita, Simulation of the spontaneous growth of a dynamic crack without constraints on the crack tip path, *Geophys. J. Int.*, *139*, 345–358, 1999a.

Kame, N., and T. Yamashita, A new light on arresting mechanism of dynamic earthquake faulting, *Geophys. Res. Lett.*, *26*, 1997–2000, 1999b.

Kame, N., J. R. Rice, and R. Dmowska, Effects of pre-stress state and propagation velocity on dynamic fault branching, *Eos Trans. AGU*, *82*(47), Fall Meet. Suppl., Abstract S22B-0648, 2001.

King, G. C. P., Speculations on the geometry of the initiation and termination processes of earthquake rupture and its relation to morphology and geological structure, *Pure Appl. Geophys.*, *124*, 567–585, 1986.

King, G., and J. Nabelek, Role of fault bends in the initiation and termination of earthquake rupture, *Science*, *228*, 984–987, 1985.

King, G., and G. Yielding, The evolution of a thrust fault system: Processes of rupture initiation, propagation and termination in the 1980 El Asnam (Algeria) earthquake, *Geophys. J. R. Astron. Soc.*, *77*, 915–933, 1984.

Knuepfer, P. L. K., Implications of the characteristics of end-points of historical surface fault ruptures for the nature of fault segmentation, *U.S. Geol. Surv. Open File Rep., 89-315*, 193–228, 1989.

Koller, M. G., M. Bonnet, and R. Madariaga, Modeling of dynamical crack propagation using time-domain boundary integral equations, *Wave Motion*, *16*, 339–366, 1992.

Kostrov, B. V., Unsteady propagation of longitudinal shear cracks, *J. Appl. Math. Mech.*, *30*, 1241–1248, 1966.

Kostrov, B. V., On the crack propagation with variable velocity, *Int. J. Fract.*, *11*, 47–56, 1975.

Kostrov, B. V., and L. V. Nikitin, Some general problems of mechanics of brittle fracture, *Arch. Mech. Stosowanej*, *22*, 749–775, 1970.

Magistrale, H., 3D simulations of discontinuous thrust faults with orthogonal segmentation, *Eos Trans. AGU*, *81*(48), Fall Meet. Suppl., Abstract S72D-05, 2000.

Magistrale, H., and S. Day, 3D simulations of multi-segment thrust fault rupture, *Geophys. Res. Lett.*, *26*, 2093–2096, 1999.

Niazi, M., Source dynamics of the Dasht-e-Bayaz earthquake of August 31, 1968, *Bull. Seismol. Soc. Am.*, *59*, 1843–1861, 1969.

Palmer, A. C., and J. R. Rice, The growth of slip surfaces in the progressive failure of over-consolidated clay, *Proc. R. Soc. London, Ser. A*, *332*, 527–548, 1973.

Power, W. L., T. E. Tullis, and J. D. Weeks, Roughness and wear during brittle faulting, *J. Geophys. Res.*, *93*, 15,268–15,287, 1988.

Ravi-Chandar, K., and W. G. Knauss, An experimental investigation into dynamic fracture, I, Crack initiation and crack arrest, *Int. J. Fract.*, *25*, 247–262, 1984a.

Ravi-Chandar, K., and W. G. Knauss, An experimental investigation into dynamic fracture, II, Microstructural aspects, *Int. J. Fract.*, *26*, 65–80, 1984b.

Ravi-Chandar, K., and W. G. Knauss, An experimental investigation into dynamic fracture, III, Steady state crack propagation and crack branching, *Int. J. Fract.*, *26*, 141–154, 1984c.

Rice, J. R., The mechanics of earthquake rupture, in *Physics of the Earth's Interior*, edited by A. M. Dziewonski and E. Boschi, *Proc. Int. Sch. Phys. Enrico Fermi*, *78*, 555–649, 1980.

Rice, J. R., Low-stress faulting: Strong but brittle faults with local stress concentrations, *Eos Trans. AGU*, *77*(46), Fall Meet. Suppl., F471, 1996.

Rice, J. R., Fracture energy of earthquakes and slip-weakening rupture parameters, *Eos Trans. AGU*, *81*(48), Fall Meet. Suppl., Abstract T21G-01, 2000.

Rice, J. R., New perspectives in crack and fault dynamics, in *Mechanics for a New Millennium: Proceedings of the 20th International Congress of Theoretical and Applied Mechanics, Chicago, Illinois, USA, 27 August–2 September 2000*, edited by H. Aref and J. W. Phillips, pp. 1–23, Kluwer Acad., Norwell, Mass., 2001.

Rice, J. R., and M. P. Cleary, Some basic stress-diffusion solutions for fluid-saturated elastic porous media with compressible constituents, *Rev. Geophys.*, *14*, 227–241, 1976.

Rubin, A. M., and C. B. Parker, Near-tip stress fields for dynamically propagating mode-II fractures, in *The Mechanical Involvement of Fluids in Faulting, U.S. Geol. Surv. Open File Rep., 94-228*, 399–405, 1994.

Savage, J. C., D. A. Lockner, and J. D. Byerlee, Failure in laboratory fault models in triaxial tests, *J. Geophys. Res.*, *101*, 22,215–22,224, 1996.

Seelig, T., and D. Gross, On the interaction and branching of fast running cracks—A numerical investigation, *J. Mech. Phys. Solids*, *47*, 935–952, 1999.

Sharon, E., S. P. Gross, and J. Fineberg, Local crack branching as a mechanism for instability in dynamic fracture, *Phys. Rev. Lett.*, *74*, 5096–5099, 1995.

Sharon, E., S. P. Gross, and J. Fineberg, Energy dissipation in dynamic fracture, *Phys. Rev. Lett.*, *76*, 2117–2120, 1996.

Sibson, R. H., Stopping of earthquake ruptures at dilational fault jogs, *Nature*, *316*, 248–251, 1985.

Sibson, R. H., Rupture interactions with fault jogs, in *Earthquake Source Mechanics, Geophys. Monogr. Ser.*, vol. 37, edited by S. Das, J. Boatwright, and C. H. Schlotz, pp. 157–167, AGU, Washington, D. C., 1986.

Sowers, J. M., J. R. Unruh, W. R. Lettis, and T. D. Rubin, Relationship of the Kickapoo fault to the Johnson Valley and Homestead Valley Faults, San Bernandino County, California, *Bull. Seismol. Soc. Am.*, *84*, 528–536, 1994.

Tada, T., and T. Yamashita, The paradox of smooth and abrupt bends in two-dimensional in-plane shear-crack mechanics, *Geophys. J. Int.*, *127*, 795–800, 1996.

Tada, T., and T. Yamashita, Non-hypersingular boundary integral equations for two-dimensional non-planar crack analysis, *Geophys. J. Int.*, *130*, 269–282, 1997.

Tada, T., E. Fukuyama, and R. Madariaga, Non-hypersingular boundary integral equations for 3-D non-planar crack dynamics, *Comput. Mech.*, *25*, 613–626, 2000.

Tsutsumi, H., and R. S. Yeats, Tectonic setting of the 1971 Sylmar and 1994 Northridge earthquakes in the San Fernando Valley, California, *Bull. Seismol. Soc. Am.*, *89*, 1232–1249, 1999.

Wallace, R. E., and H. T. Morris, Characteristics of faults and shear zones in deep mines, *Pure Appl. Geophys.*, *124*, 107–125, 1986.

Wong, T. F., Shear fracture energy of Westerly granite from post-failure behavior, *J. Geophys. Res.*, *87*, 990–1000, 1982.

Xu, X.-P., and A. Needleman, Numerical simulations of fast crack growth in brittle solids, *J. Mech. Phys. Solids*, *42*, 1397–1434, 1994.

Yeats, R. S., G. J. Huftile, and L. T. Stitt, Late Cenozoic tectonics of the east Ventura basin, Transverse Ranges, California, *AAPG Bull.*, *78*, 1040–1074, 1994.

Yoffe, E. H., The moving Griffith crack, *Philos. Mag.*, *42*, 739–750, 1951.

R. Dmowska and J. R. Rice, Department of Earth and Planetary Sciences and Division of Engineering and Applied Sciences, Harvard University, Cambridge, MA 02138, USA. (rice@esag.Harvard.edu)

A. N. B. Poliakov, Laboratoire de Geophysique et Tectonique, CNRS case 060, Université Montpellier II, F-34095, Montpellier Cedex 5, France.